ACS OMEGA

http://pubs.acs.org/journal/acsodf

Article

Experimental and Quantum Chemical Study on the Inhibition Characteristics of Glutathione to Coal Oxidation at Low Temperature

Yujia Huo and Hongqing Zhu*

Cite This: *ACS Omega* 2022, 7, 31448−31465

Read Online

ACCESS | Metrics & More | Article Recommendations

ABSTRACT: In response to the frequent occurrence of coal spontaneous combustion accidents, this paper proposes to use glutathione (GSH) as an inhibitor to inhibit the coal oxidation at low temperature. Based on the gas production of oxidation, thermogravimetric analysis, electron spin resonance, and in situ Fourier infrared transform spectroscopy experiments, it is known that GSH has a good inhibiting effect on lignite, long-flame coal, and fatty coal. The optimal action temperature of GSH is 60−150 °C, which can effectively slow down the weight loss and exothermic process and reduce the gas production of CO and CO_2. Compared with the raw coal, the GSH-treated coal samples possess higher crossing point temperature and lower reactive group content. Subsequently, quantum chemical calculations are performed using density functional theory. The results demonstrate that the inhibiting mechanism of GSH is inerting the reactive radicals in coal and converting them into more stable compounds. Meanwhile, the activation energy of the reaction between GSH and each reactive radical is small, and all of them can occur at room temperature and pressure. This study lays the groundwork for future development of inhibitors.

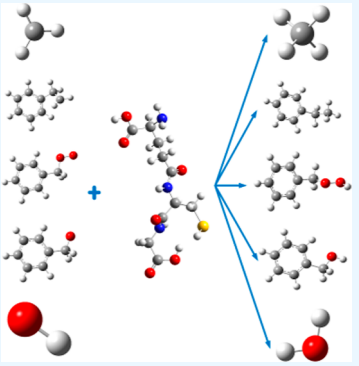

1. INTRODUCTION

Coal is one of the major fossil energy sources in the world, dominating the energy consumption of all countries and influencing the industrialization process of society at all times.[1−4] Nonetheless, owing to the depth of coal mining increases, the geothermal influence is progressively enlarging and coal spontaneous combustion accidents occur now and again.[5−9] Serious coal spontaneous combustion accidents not only lead to the waste of coal resources and increase the pressure on environmental protection but also cause irreversible damage to equipment, while critically threatening the personal and property safety of operators.[10,11] Consequently, it is of great practical significance to take necessary and effective measures to prevent and control coal spontaneous combustion and ensure coal mine safety production.

In order to reduce the occurrence of coal spontaneous combustion disasters, a large number of scholars have carried out research on the mechanism of coal spontaneous combustion. Currently, the coal−oxygen complex theory is the most widely accepted.[12−14] This theory holds that coal spontaneous combustion disasters occur due to physical[15] and chemical[16] adsorption of O_2 by coal at normal atmospheric temperature, which in turn leads to oxidative autothermal reactions.[17] The coal oxidation at low temperature (COLT) plays a key role in the process, so it is particularly important to regulate the oxidative exotherm of coal in the low temperature stage.[18]

Based on the theory of COLT, scholars have carried out a lot of research on coal spontaneous combustion prevention and control technology, which can be broadly divided into physical and chemical inhibition methods.[19] Physical inhibition methods mainly include grouting,[20] inert injection,[21,22] foam gel,[23,24] and physical inhibitors.[25,26] These methods aim to absorb heat or exclude oxygen to play a role in inhibiting the COLT, whereas there are certain limitations. The disadvantage of the grouting method is the poor fluidity, and the slurry is difficult to be accurately transported to the high-temperature area, resulting in low resistance. The carrier of the inert gas in the inert injection method is the fresh air flow, the isolation of oxygen is not effective, and the sealing of the area is a high requirement. The foam gel method has poor stability, and it is difficult to make the foam adhere to the coal surface for a long time. Physical inhibitors mainly consist of NaCl,[27] $MgCl_2$,[28] $CaCl_2$,[29] and ammoniums,[30,31] which have poor thermal stability and a poor inhibiting effect in the high temperature stage. Additionally, they are susceptible to generating toxic and harmful gases such as HCl and NH_3, which pose a threat to the

Received: June 20, 2022
Accepted: August 15, 2022
Published: August 24, 2022

https://doi.org/10.1021/acsomega.2c03861
ACS Omega 2022, 7, 31448−31465

Table 1. Proximate, Ultimate, and Calorific Value Analysis of Three Coal Samples[a]

	proximate analysis					calorific value	ultimate analysis				
coal samples	M_{ad} (%)	A_{ad} (%)	V_{ad} (%)	V_{daf} (%)	FC_{ad} (%)	$Q_{b,ad}$ (kJ/kg)	C (%)	H (%)	O (%)	N (%)	S (%)
XL	10.72	17.11	39.26	40.33	32.94	19.77	56.44	4.12	19.76	0.48	0.85
DH	3.08	8.04	33.46	35.21	54.31	28.46	80.70	3.98	9.46	1.40	1.41
FL	2.75	9.74	28.94	30.08	60.55	34.13	79.29	5.37	10.24	1.36	1.30

[a]ad, air dry basis.

health of the staff. Chemical inhibitors are predominantly antioxidants, which can be divided into free radical scavengers, hydroperoxide decomposers, free radical quenchers, metal chelating agents, and so forth.[32] Their mechanism is to inert reactive free radicals, which can fundamentally inhibit the COLT.[31,33,34] Li et al.[19] proposed 2,2,6,6-tetramethyl-1-piperidine-noxyl (TEMPO), butylated hydroxytoluene, VC, triphenyl phosphite, edetic acid, and phytic acid as new inhibitors from the perspective of inhibiting chain reactions, which showed that they all have certain inhibiting effects and TEMPO had the best inhibiting effects.[35] Lu et al.[36] investigated the inhibiting properties of environment-friendly DL-malic acid on lignite and bituminous coal. They affirmed that the DL-malic acid-treated coal samples had elevated crossing point temperature (CPT) and lower typical gas yields and were more potent for water-soaked coal. Liu[37] explored the inhibiting effects of citric acid on coal spontaneous combustion. The results illustrated that the addition of citric acid could essentially reduce the catalytic effect of metal ions in raw coal on coal spontaneous combustion, and it has good general applicability to coals with different degrees of metamorphism. Dou et al.[38] summarized the inhibiting effects of catechin with different concentrations and observed that the inhibiting mechanism was to accelerate the formation of stable ether bonds in the coal, and the best inhibiting effects was achieved when the concentration of catechin was 10%.

In spite of research on antioxidants having been performed, previous research has only briefly discussed the inhibiting effects, and the knowledge of the inhibiting mechanism is only at the macro level, lacking comprehensive and in-depth research at the micro level. As a matter of fact, the essential study of macro combined with micro is also surprisingly limited. In addition, the selection of inhibitors is poorly targeted, the identification of determinant reactive groups is missing, and there is a significant lack of research correlating the inhibiting effects with the chemical structures change in the coal. Wang,[39] Qi,[39] and Zhu et al.[40−42] established and refined the chain reaction model of COLT, and the results demonstrated that alkyl radicals, alkoxy radicals, hydroxyl radicals, and peroxyl radicals are the main reactive substances. Accordingly, the search for an inhibitor that could inert them is a top priority of current research. Reduced glutathione (GSH) is a broad-acting physiological factor, a tripeptide composed of glutamic acid, cysteine, and glycine, which is widely distributed in organisms such as tomato and sweet potato and has highly effective antioxidant properties.[43] In the pharmaceutical field, GSH is often used as a therapeutic agent for hepatitis and hemolytic diseases. It could participate in the tricarboxylic acid cycle in the body to activate various enzymes. Moreover, it has inhibiting effects on unstable ocular lens protein sulfhydryl groups and plays a powerful regulator in maintaining cellular physiological functions.[44] In food processing, GSH is utilized as a base for functional foods, acting as a stabilizer and improving the flavor.[45] In medical aesthetics, GSH has anti-ageing, whitening, and immune enhancing effects.[46] Paradoxically, the application of GSH in the mining industry is limited, and its inhibiting effects on coal spontaneous combustion remains much less explored.

In this study, three coal samples with different degrees of metamorphosis were administered as research objects. Experimental methods, for instance, gas production of oxidation, thermogravimetry analysis differential scanning calorimetry (TG−DSC), electron paramagnetic resonance (EPR), and in situ Fourier transform infrared (FTIR) spectroscopy, were applied to disclose the law of weight loss and heat release, gas composition and yield, surface functional group composition, and free radical changes of the coal samples before and after GSH treatment and to evaluate the inhibiting effects of GSH.

2. EXPERIMENTS AND CALCULATIONS

2.1. Experiments. In order to accurately analyze the inhibiting characteristics of GSH to COLT, three coal samples with different degrees of metamorphism, namely, the Xilingol coal sample from Inner Mongolia, the Douhou coal sample from Hebei, and the Fuli coal sample from Heilongjiang, were selected. The proximate analysis was completed in accordance with GB/T30732-2014, the ultimate analysis was carried out in accordance with GB/T476-2008, and the heat generation was tested on an oxygen bomb calorimeter according to GB/T213-2008. The results are shown in Table 1.

2.1.1. Coal Sample Preparation. First, appropriate coal samples were gathered and vacuum-sealed; second, the oxidized parts were removed under nitrogen protection to obtain fresh cores, which were broken into small pieces after the samples were delivered to the laboratory; subsequently, small coal pieces were further ground using a ball mill and the pulverized coal in the particle size range of 0.18−0.25 mm was obtained; and eventually, the pulverized coal was dried in a vacuum-drying oven at 30 °C for 24 h and was sealed in a glass jar to prevent oxidation. After the preparation of the pulverized coal, 50 g of each of the three types of pulverized coal was soaked in aqueous GSH solution with a mass fraction of 5% (where the mass of GSH is 2.5 g and the mass of water is 47.5 g) and stirred well, then, the solution was left to stand for 48 h. The pulverized coal was then filtered through filter paper and dried in a vacuum-drying oven at 40 °C for 24 h. Finally, the three types of pulverized coal were stored in sealed bags and labeled as GSH-XL, GSH-DH, and GSH-FL, respectively. For comparative analysis, the same method was used to prepare the raw coal samples, with the exception that the 5% aqueous GSH solution was replaced with water and labeled raw-XL, raw-DH, and raw-FL, respectively.

2.1.2. Gas Production of the Oxidation Experiment. The oxidation gas production experiment allows the study of gas products and CPTs during the heating process of raw coal and suppressed samples. Before the experiment, the gas tightness of

https://doi.org/10.1021/acsomega.2c03861
ACS Omega 2022, 7, 31448−31465

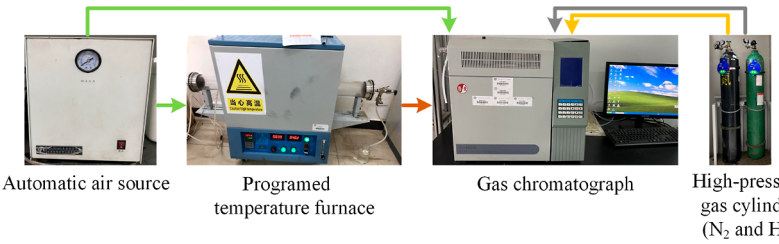

Figure 1. Devices and process of the gas production of the oxidation experiment.

the apparatus was checked. 150 g of the prepared sample was weighed and placed in the reaction furnace, and a thermocouple was placed in the center of the sample to monitor the temperature. During the experiment, pure air was continuously injected at a flow rate of 60 mL/min. The reaction furnace was heated from 30 to 200 °C, administering a heating procedure at a rate of 2 °C/min. For every 5 °C increase of the temperature, the gases were fed into the gas chromatograph to test the gases' concentration. The coal oxidation generates a variety of gases, such as CO, CO_2, C_2H_4, H_2, CH_4, and so forth. The gases could change with the increase of temperature and the degree of coal metamorphism and can also be used to evaluate the coal oxidation degree.[47] It is worth noting that to ensure the accuracy of the gas chromatograph, the procedure was retained at a constant temperature for 20 min at each detection temperature point during the test. The experimental devices are illustrated in Figure 1.

2.1.3. TG–DSC Experiment. The TG–DSC technique is an operative means of studying and testing the exothermic properties of coal oxidation and was selected in this study to analyze the inhibiting effects of GSH. The experiments were carried out in the STA-449-F3 thermal analyzer from NETZSCH company, Germany. The mass, temperature, and sensitivity of the instrument were calibrated before the experiments utilizing the program provided by NETZSCH company, with the mass accuracy controlled to 0.1 μg and the temperature accuracy controlled to ±0.1 °C. Each sample was placed in an alumina crucible with a mass of 10 mg, where the drying air flow rate was controlled at 60 mL/min, the coal heating rate was controlled at 2 °C/min, and the heating temperature range was from 30 to 500 °C.

2.1.4. EPR Test. The nature of free radicals can be studied using the EPR test,[48] and in this paper, we compared the inhibiting effects of GSH at different temperatures. The test was accomplished on the Bruker EMXplus EPR tester from Germany. Due to the complex structure of coal, the peaks of the solid-state EPR spectrum of 1,1-diphenyl-2-trinitrophenyl hydrazine (g = 2.0036) is comparable to that of coal and its g value is also comparatively close, so 1,1-diphenyl-2-trinitrophenyl hydrazine was used as a standard sample of solid radicals in this experiment.[49] After taking 20 mg of 1,1-diphenyl-2-trinitrophenylhydrazine for EPR benchmark calibration, 20 mg of the coal sample was weighed and heated to 30, 90, 150, and 210 °C for detection. The instrument parameters were set as follows: the microwave frequency was 9.8 ± 10-8 GHz, the microwave power was 4 mW, the central magnetic field was 3510 ± 10^{-6} G, the scan width was 70 G, the time constant was 5.12 ms, the scan time was 20.97 s, the modulation amplitude was 1 G, and the modulation frequency was 100 KHz.

2.1.5. In Situ FTIR Test. In this paper, raw and inhibited coal samples were tested using a Thermo IS 50 in situ FTIR spectrometer. In order to exclude the interference from the diluent, a base vector acquisition of pure KBr was executed in the diffuse reflection test mode as a reference. The sample was weighed to be 0.001 g, blended with KBr powder in the ratio of 1:150, and ground for 20 min. The well-milled powder was loaded into the press and pressurized to 10 MPa, and the film was removed after 1 min to obtain a transparent sheet 0.9 mm in diameter and 0.1 mm in thickness. Then, the transparent sheet was loaded into the sample chamber for scanning in a wavenumber range of 4000–400 cm^{-1} and at a resolution of 4.0 cm^{-1}, with a total scanning number of 64. During the test, dry air was continuously introduced, the flow rate was 60 mL/min, the test temperature range was 30–200 °C, the temperature increase rate was 2 °C/min, and the data were collected when the temperature increased to 40, 80, 120, 160, and 200 °C.

2.2. Quantum Chemical Calculations. According to the free radical reaction theory, the COLT is a chain reaction process, which can be divided into chain initiation, chain propagation, and chain termination stages.[50] In the chain initiation stage, the primary coal generates a large amount of R–$^{\bullet}CH_2$ and $^{\bullet}CH_3$ under the mechanical damage or geothermal heat. Once the radicals come into contact with O_2, the chemisorption reactions occur to generate ROO$^{\bullet}$ radicals. In the chain propagation stage, ROO$^{\bullet}$ radicals continue to participate in the oxidation reaction and indirectly generate reactive groups such as $^{\bullet}$OH and RO$^{\bullet}$. In the chain termination stage, the reactive radicals bind to each other to generate inert substances. As a consequence, reactive radicals in the chain initiation and chain propagation stages, including R–$^{\bullet}CH_2$, $^{\bullet}CH_3$, ROO$^{\bullet}$, RO$^{\bullet}$ and $^{\bullet}$OH, were mainly considered in this study. GSH is a free radicals adsorbent that can inert or scavenge reactive radicals, thus considerably reducing the number of reactive sites on the coal surface. Furthermore, GSH itself can generate inert GSSH, hence terminating the continuation of the oxidation reactions. In order to investigate the reaction mechanism of GSH inerting reactive radicals, various molecular models were established in Gauss View 6.0 software, and quantum chemical calculations were executed using the density functional theory (DFT) in Gaussian 16W.

2.2.1. Calculation Contents. As we all know, the coal macromolecular model is very intricate. According to previous studies, the coal molecule can be simplified by the combination of a benzene ring and a functional group.[51] As a result, Ar–CH_2–$^{\bullet}CH_2$, $^{\bullet}CH_3$, Ar–CH_2–OO$^{\bullet}$, Ar–CH_2–O$^{\bullet}$, and $^{\bullet}$OH can be constructed as the molded compounds of the five reactive groups, and the inhibiting reaction pathways for COLT of GSH can be envisioned as Reaction 1.[44]

https://doi.org/10.1021/acsomega.2c03861
ACS Omega 2022, 7, 31448–31465

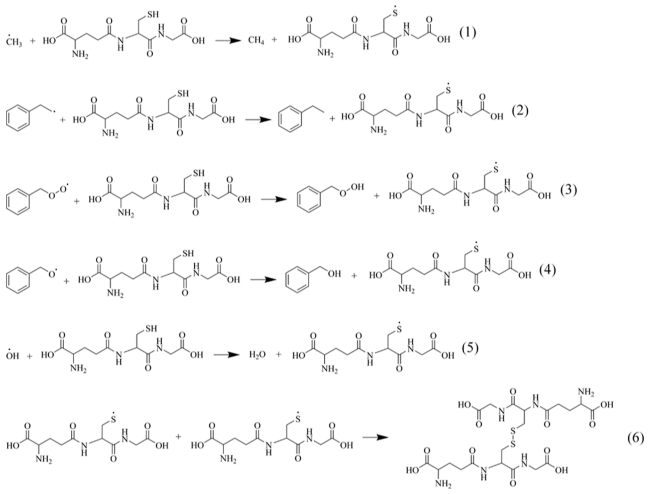

2.2.2. Molecular Structure Optimization. We applied the M062X method in DFT to describe the electronic exchange and selected the 6-311G(d, p) basis group for dispersion correction by merging the Becke−Johnson damping function with Grimme's DFT-D3 algorithm.[52,53] The molecules were optimized using the ground state method, and the orbital distribution and electron delocalization were analyzed using natural bond orbitals (NBOs). Subsequently, the molecular electrostatic potential (ESP) was employed to predict the reaction centers.[54] The TS (Berny, QST2) method was chosen to search the transition states, and the reaction pathways were verified using the intrinsic reaction coordinate (IRC) method.[17] It is worth noting that the spin multiplicity can be obtained by calculating the number of α electrons minus the number of β electrons plus 1.

2.2.3. Calculation of Thermodynamic Parameters. Enthalpy (H) and Gibbs free energy (G) are important characteristic parameters in thermodynamics for the characterization of the reactivity. The enthalpy change (ΔH) is the difference between the H of the product and the reactant, and the activation energy (ΔE) can be defined as the difference between the G of the transition state and the reactant, that is, the maximum energy barrier to be overcome for the reaction to occur.[55] When $\Delta H > 0$, the reaction is endothermic; when $\Delta H < 0$, the reaction is exothermic; when $\Delta E > 0$, the reaction is non-spontaneous (heat absorption required); and when $\Delta E < 0$, the reaction is spontaneous (no heat absorption required). Based on this theory, the thermodynamics parameters of the proposed reactions were calculated.

3. RESULTS AND DISCUSSION

3.1. Gas Production of Oxidation Analysis. In the initial stage of heating, the sample center temperature is lower than that of reaction furnace, then with the transfer of instrument heat and coal oxidation, the temperature of the sample center stars to increase, and it must be higher than that of the reaction furnace at a certain point, which is called the CPT. Consequently, the CPT can be applied as an auxiliary indicator to judge the inhibiting ability of antioxidants, and the higher the CPT, the better the inhibiting effects.[35] Table 2 shows the CPTs of different samples. It can be observed that the CPT of the raw-XL sample is 120.1 °C and that of the GSH-XL sample is 132.6 °C, indicating that the addition of GSH delays the CPT of raw-XL sample by 12.5 °C. Similarly, the CPTs of DH and FL samples are delayed by 8.4 and 6.2 °C. Through combined analyses of data from all samples, it can be realized that GSH has an effective inhibiting effect on COLT.

Table 2. CPTs of Samples

samples	raw-XL	GSH-XL	raw-DH	GSH-DH	raw-FL	GSH-FL
CPT	120.1	132.6	132.7	141.1	139.6	145.8

CO and CO_2 are typical gases produced during the COLT and can be used to evaluate the oxidation degree. Simultaneously, O_2 consumption is normally used as an effective indicator to assess the effects of the inhibitor. In this context, we measured the variation of the CO and CO_2 release and the O_2 consumption of each sample with temperature increase through gas chromatography, and the variation curves are shown in Figure 2.

It is detected that the released CO of all three samples increases with temperature increase before and after inhibition, but the differences are not significant before 70 °C. Nevertheless, the CO release of the inhibited coal samples are significantly lower than those of the raw coal samples after 70 °C. To summarize, the reason for this phenomenon is the formation of the free radical chain reactions, and CO is the product of reactive free radicals. At the same temperature, the CO_2 release is considerably lower than that of CO, but the variation curve is similar to that of CO. Homoplastically, the CO_2 release of the inhibited sample is also markedly lower than that of the raw coal from 70 °C. According to the O_2 consumption variation curves, the O_2 concentrations of the three inhibited samples are higher than those of the raw coal samples at the same temperature. The O_2 contents of the raw and inhibited coal samples do not differ significantly between 30 and 70 °C. However, with the increase of temperature, the oxidation reaction rate of coal accelerates, and the O_2 content of raw coal samples starts to decrease significantly after 70 °C, while the decrease of inhibited coal samples is less, indicating that GSH could effectively reduce the O_2 consumption of coals with different degrees of metamorphism. Equally, these observations demonstrate that the O_2 content of the GSH-XL sample is higher than those of GSH-DH and GSH-FL samples. As described above, GSH serves this function of inhibiting the release of CO and CO_2 and the consumption of O_2, which can undermine the oxidation of lignite, long-flame coal, and fatty coal.

The inhibition rate can effectively characterize the inhibiting effects of inhibitors, and the higher the inhibition rate, the stronger the ability of the inhibitor.[28] In order to further quantify the inhibiting effects of GSH during the COLT, the CO released is chosen as the characterization parameter, and the GSH inhibition rate variation curves are compared and analyzed. The inhibition rate at a specified temperature can be computed using the following equation.

$$r(t) = \frac{w_1(t) - w_2(t)}{w_1(t)} \tag{2}$$

where $r(t)$ is the inhibition rate at t °C, given in percentage; $w_1(t)$ is the CO release of the raw coal sample at t °C, given in parts per million; and $w_2(t)$ is the CO release of the raw coal sample at t °C, given in parts per million.

Figure 3 depicts the inhibition rate variation of GSH for the three coal samples with increasing temperature. These data reveal that GSH has good inhibiting effects on all three samples, but the distributions of the inhibition rate are not the same. Overall, GSH shows the highest inhibition rate for the

https://doi.org/10.1021/acsomega.2c03861
ACS Omega 2022, 7, 31448−31465

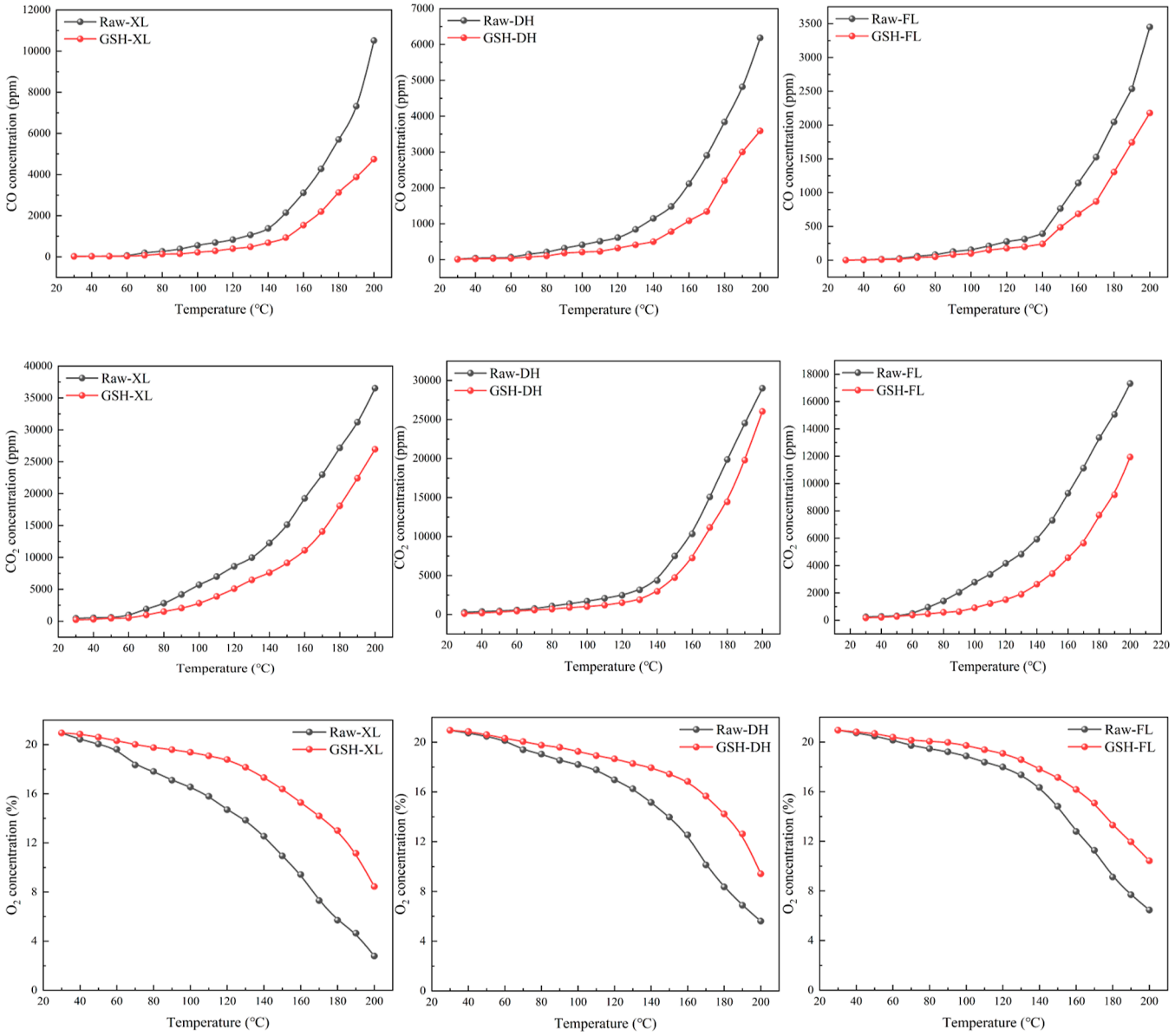

Figure 2. CO and CO_2 emission and O_2 consumption of different samples with increasing temperature.

XL coal sample, followed by the DH coal sample, and shows the lowest rate for the FL coal sample. The inhibition rates of all three samples are unpredictable and fluctuate before 60 °C. As the temperature increases, they are comparatively stable in the range of 60−150 °C and are distributed in the ranges of 52−63%, 42−56%, and 27−38%, respectively. After 150 °C, they continue to produce fluctuations. These results assume that the main action temperature of GSH is distributed in 60−150 °C, and the lower the degree of coal deterioration, the better the inhibiting effects of GSH. This phenomenon can be explained as follows: it is well-known that coal with a lower degree of metamorphism has more reactive free radicals and a higher propensity to spontaneous combustion. Based on the results of proximate and ultimate analysis, XL coal contains the most reactive free radicals due to the lowest rank of metamorphism, DH coal has the second highest reactive free radicals content, and FL coal has the lowest reactive free radicals content with the highest rank of metamorphism. Meanwhile, the inhibition mechanism of GSH to the COLT is inerting reactive radicals, so the lower the free radical content is, the less effective the GSH is. As a result, it has the highest inhibition rate for XL coal containing the most reactive free radicals, followed by DH coal, and has the lowest rate for FL coal.

3.2. TG−DSC Analysis. Figures 4−6 show the TG, differential TG (DTG), and DSC curves of the raw coal and inhibited samples of XL, DH, and FL, respectively. As can be seen from the figures, this heating process can all be divided into four stages: gas desorption, oxygen absorption, pyrolysis, and combustion stages.[9] In the gas desorption stage, the water and adsorbed gas in the coal progressively evaporate and desorb with the increase of temperature, and the TG curve has an obvious decreasing trend. The slight mass increase of the sample during the oxygen absorption stage is attributed to the chemisorption reaction of O_2 with the reactive groups on the coal surface. The mass of the sample keeps decreasing during the pyrolysis stage, accompanied by the release of volatile gases and the pyrolysis of unstable oxygenated compounds. During the combustion stage, the sample undergoes a turbulent oxidative exothermic reaction with a rapid mass decrease.

https://doi.org/10.1021/acsomega.2c03861
ACS Omega 2022, 7, 31448−31465

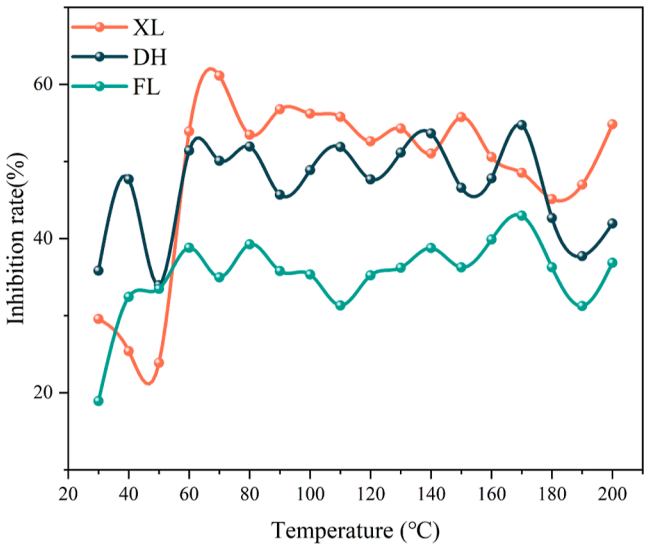

Figure 3. Variation curves of inhibition rates of the samples.

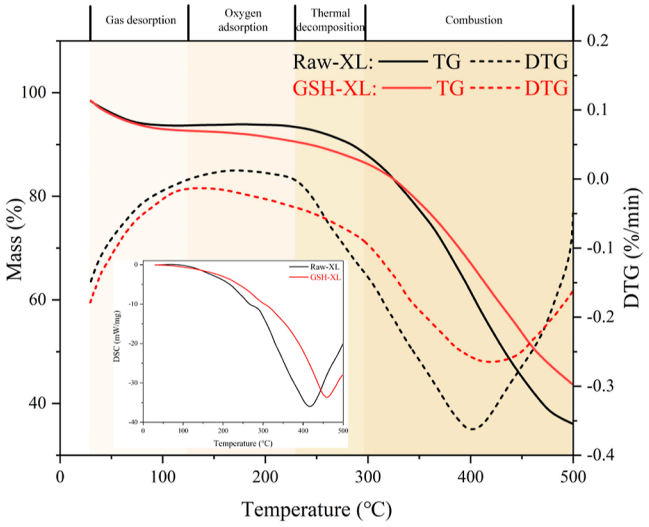

Figure 4. TG−DTG and DSC curves of raw-XL and GSH-XL samples.

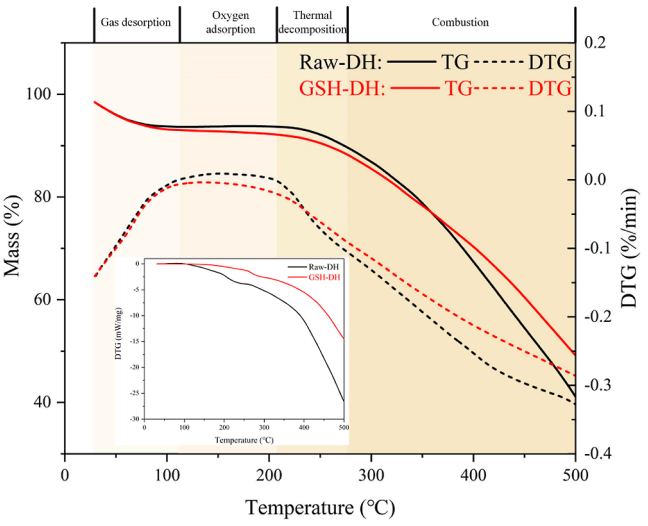

Figure 5. TG−DTG and DSC curves of raw-DH and GSH-DH samples.

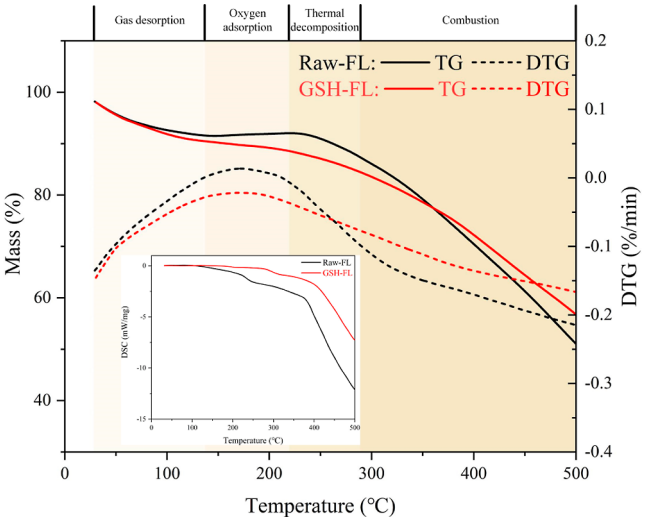

Figure 6. TG−DTG and DSC curves of raw-FL and GSH-FL samples.

From the TG and DTG curves of the raw-XL and GSH-XL samples, it can be observed that the TG curve of the raw-XL sample steadily decreases with the increasing temperature until 123 °C, which is the gas desorption stage. This phenomenon can be largely explained by the evaporation of water from the sample, the desorption of adsorbed gases in the pore and fissures (CO_2, CH_4, etc.), and the escape of oxidized gases at low temperatures. In the range of 123−258 °C, the mass of the raw coal sample increases gently due to the oxygen absorption. As the temperature elevates, the raw coal sample enters the pyrolysis stage, during which the aromatic ring structure in the sample undergoes a cleavage reaction, generating a large amount of volatiles and heat, and the mass minimizes rapidly. At 291 °C, the sample reaches the ignition point and enters the combustion stage, and the weight loss becomes swifter. Soon afterward, the oxidation reaction is the most intense at 401 °C with the maximum weight loss rate. After 401 °C, the weight loss rate gradually decreases, and the reaction weakens step by step. Comparing with that of the raw-XL sample, the trend of the TG curve of the GSH-XL sample is fundamentally comparable, which continues to decrease with increasing temperature. In the gas desorption stage, the GSH-XL sample has a greater mass loss, presumably originating from the reduction of $^{\bullet}CH_3$ to CH_4. In contrast, there is no weight gain during the oxygen absorption stage of the GSH-XL sample, indicating that GSH can effectively weaken the adsorption and transport of O_2. After 256 °C, the weight loss rate of the GSH-XL sample starts to be smaller than that of the raw-XL sample, and the ignition point temperature of the GSH-XL sample is shifted to the high temperature region by 38 °C. It is noteworthy that the weight loss rate reaches the maximum at 424 °C, which is delayed by 23 °C compared with that of the raw-XL sample.

The TG curves of the raw-DH and raw-FL samples are similar to those of the raw-XL sample, whereas the ignition point temperatures of the inhibited samples are delayed by 19 and 11 °C, respectively. As a result of the low spontaneous combustion tendency of raw-DH and raw-FL samples, although the maximum weight loss rate is not reached before 500 °C, it is obvious that the maximum weight loss rate

https://doi.org/10.1021/acsomega.2c03861
ACS Omega 2022, 7, 31448−31465

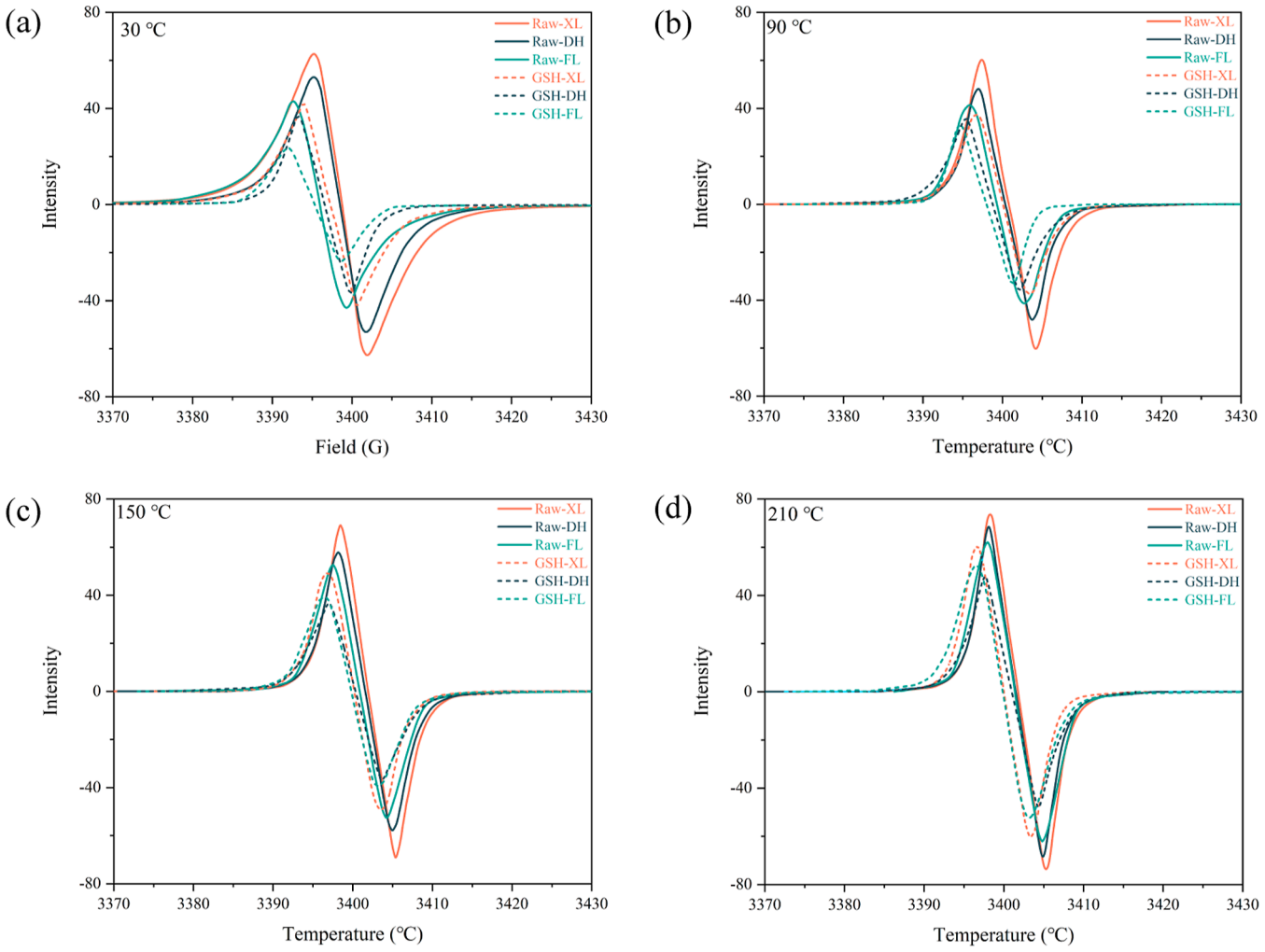

Figure 7. EPR spectra of raw and inhibited coal samples at (a) 40, (b) 90, (c) 150, and (d) 210 °C.

temperature of the inhibited samples is delayed according to the DTG curves. As described above, GSH can effectively inhibit the COLT, and it is universal for the three different ranks of coal.

The results of the DSC curves suggest that the exothermic process of each raw sample has the same variation trend, and all of them absorb heat first and then release it. The DSC curves of the inhibited samples are basically the same as that of the raw samples, but the heat releases of the inhibited samples are all smaller than that of the raw samples at the same temperature. The temperature corresponding to the maximum exothermic power of the GSH-XL sample is delayed to some extent compared with that of the raw-XL sample. Although the DH and FL samples do not reach the maximum exothermic power before 500 °C, the trend of the DSC curves shows that the temperature point corresponding to the maximum exothermic power is also delayed to some extent. Intriguingly, all the DSC curves have both an exothermic subpeak in addition to the main exothermic peak. This may be strongly associated with the intensifying effects of the temperature increase in the pyrolysis stage, some active structures are oxidized and decomposed into small molecules, and the exothermic reaction makes the heat flow power increase. Nonetheless, it can be seen that the exotherm subpeaks of the inhibited samples are significantly delayed, demonstrating that the addition of GSH slows down the oxidation reaction and weakens the oxidation of the coal.

3.3. EPR Analysis. Based on the test results, the EPR spectra of the three raw coal samples and the corresponding inhibited samples at 30, 90, 150, and 210 °C are shown in Figure 7. The free radical concentration, *g* factor, and linewidth are the main characterization parameters of the EPR experiments. The variation law of the three parameters with increasing temperature can be calculated from the raw data and are shown in Figures 8−10.

The variation pattern of free radical concentration is shown in Figure 8. It can be seen that the free radical concentrations of all three raw coal samples increase gradually with the increase of temperature, and the increasing rates slow down after 150 °C. This is because the chain reactions of the COLT have been formed at 150 °C, and the consumption and generation of free radicals tend to be stable. The raw-XL sample has the highest free radical concentration at the same temperature, followed by the raw-DH sample, and the raw-FL sample has the lowest, which is consistent with the conclusion that coals with low degrees of metamorphism possess more reactive groups. Compared with that of the raw coal samples, the free radical concentrations of the inhibited samples show the same trends with increasing temperature, but the magnitudes all decrease, indicating that the addition of GSH could reduce the free radicals in coal.

https://doi.org/10.1021/acsomega.2c03861
ACS Omega 2022, 7, 31448−31465

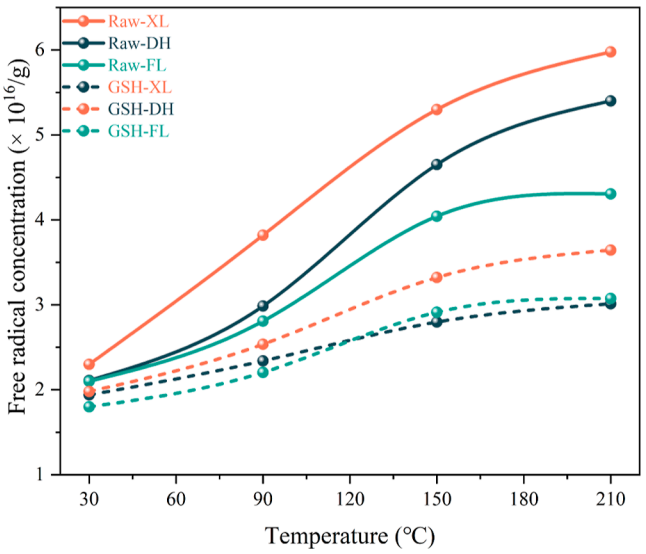

Figure 8. Variation trend of free radical concentration of raw coal and inhibited coal samples with temperature increase.

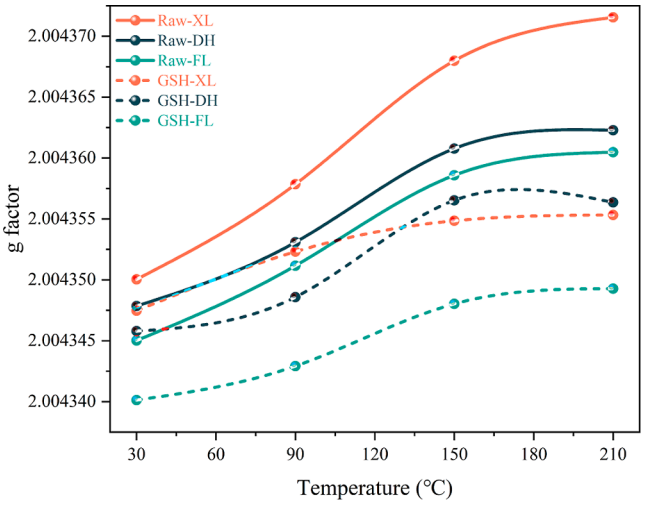

Figure 9. Variation trend of the *g* factor of raw coal and inhibited coal samples with temperature increase.

The *g* factor reflects the number of unpaired electrons in the system, and the *g* factor of coal at normal temperature and pressure is higher than the free electrons of the empty groups (g_e = 2.0023).[33] As can be seen from Figure 9, the *g* factors of the three raw coal samples also increase gradually with increasing temperature, which is due to the increase of the free radicals contributing to the ascend of the unpaired electrons. The *g* factors of all three inhibited samples are smaller than those of the corresponding raw samples at the same temperature, testifying that GSH could reduce some of the free radicals in the samples. These results reflect the inhibiting effects of GSH on the COLT.

The linewidth reports the energy exchange between the free radicals and the coal microcrystalline structure. Figure 10 shows that the linewidth of the raw samples gradually increases with the increase of temperature, mainly because the chain reactions increase the free radical contents considerably, the molecular structure becomes loose, and the spin lattice effects become weaker, which shortens the relaxation time. At the same temperature, the linewidth of each inhibited sample is

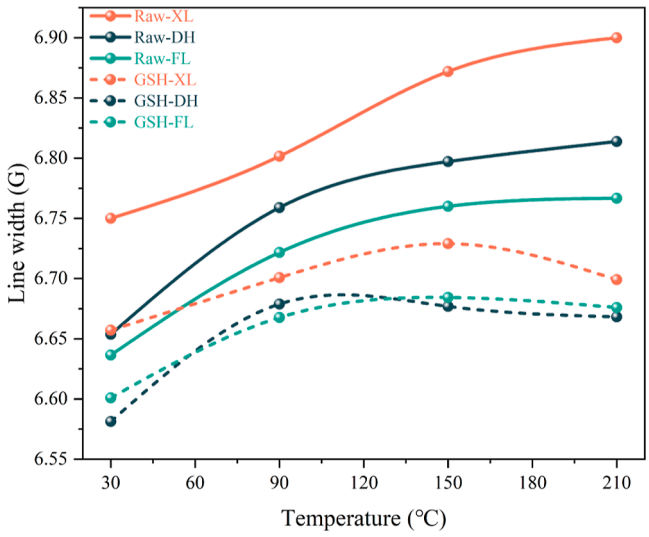

Figure 10. Variation trend of linewidth of raw coal and inhibited coal samples with temperature increase.

smaller than that of the corresponding raw sample, implying that GSH hindered the oxidation reaction and diminished the free radical concentration.

3.4. In Situ FTIR Analysis. In order to quantify the change of function group contents before and after GSH treatment, all samples were tested by the in situ FTIR method. Figure 11 displays the FTIR spectra of the raw data after smoothing, and it can be found that the spectral curves of raw samples and inhibited samples at the same temperature show obvious differences. Likewise, there are also obvious changes in the spectral curves of the same coal samples at various temperatures.

PeakFit software was applied to fit the raw spectral curves. Fourier deconvolution and Gaussian function methods were used to smooth and separate the overlapping and interfering spectral peaks to study the functional groups in the coal samples more accurately. Additionally, for the sake of the elimination of the baseline drift during the test as much as possible, the ratio of the area occupied by each peak to the total peak area was considered as its content. Based primarily on previous studies,[39] the vibrations of $-CH_3$, $-CH_2$, and $-CH$ are located in the wavenumber range of 2800−3000 cm^{-1}, and the vibrations of OH are distributed in the wavenumber range of 3000−3800 cm^{-1}. The vibrations in the wavenumber range of 1000−1800 cm^{-1} belong to oxygen-containing functional groups, which can be divided into 1000−1550 and 1550−1800 cm^{-1}, whose peaks are assigned to C−O and C═O bond vibrations, respectively. The evolution pattern of each functional group in the COLT process is shown in Figure 12.

Figure 12a shows the variation pattern of the content of alkyl groups (primarily $-CH_3$ and $-CH_2-$)with increasing temperature before and after the GSH treatment of the three coal samples. The results suggest that the alkyl group contents of the three samples are ranked as XL > DH > FL, which is consistent with the conclusion that coals with low degree of metamorphism have more alkyl group side chains. The alkyl group contents of all three raw coal samples gradually decline with increasing temperature, which is due to the oxidation of alkyl groups by O_2 to form alkyl radicals and participate in chain reactions. The variation law of alkyl group content in the

https://doi.org/10.1021/acsomega.2c03861
ACS Omega 2022, 7, 31448−31465

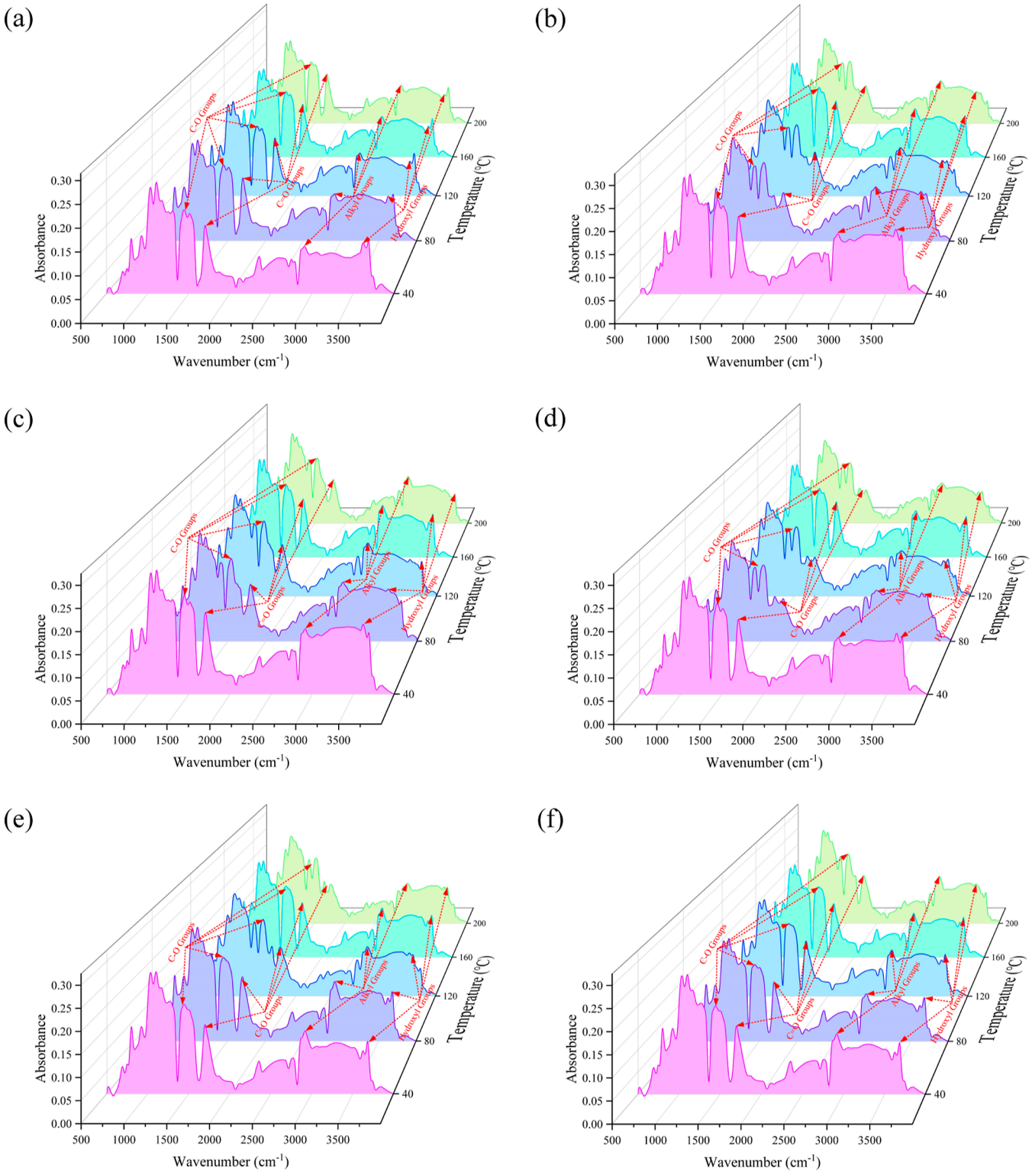

Figure 11. In situ FTIR spectra of (a) raw-XL, (b) GSH-XL, (c) raw-DH, (d) GSH-DH, (e) raw-FL, and (f) GSH-FL.

inhibited sample has the same trend as that of the raw coal sample, yet the alkyl group content is larger than that of the raw coal sample, which is due to the fact that GSH could reduce the alkyl radicals to alkyl groups, hindering the oxidation process of alkyl radicals to some extent.

Figure 12b exhibits the variation law of alkoxy groups with temperature increase before and after GSH treatment for the three coal samples. It can be found that the alkoxy group contents gradually increase as the temperature increases, which is due to the oxidation of alkyl groups. It should be noted that the alkoxy group contents of the inhibited samples increase promptly before 120 °C, but the contents at the same temperature are all smaller than those of the raw samples. This indicates that the addition of GSH can restrict the oxidation of alkoxy groups. After 120 °C, the increase rates of alkoxy groups of the inhibited samples tend to level off, which can be largely

https://doi.org/10.1021/acsomega.2c03861
ACS Omega 2022, 7, 31448−31465

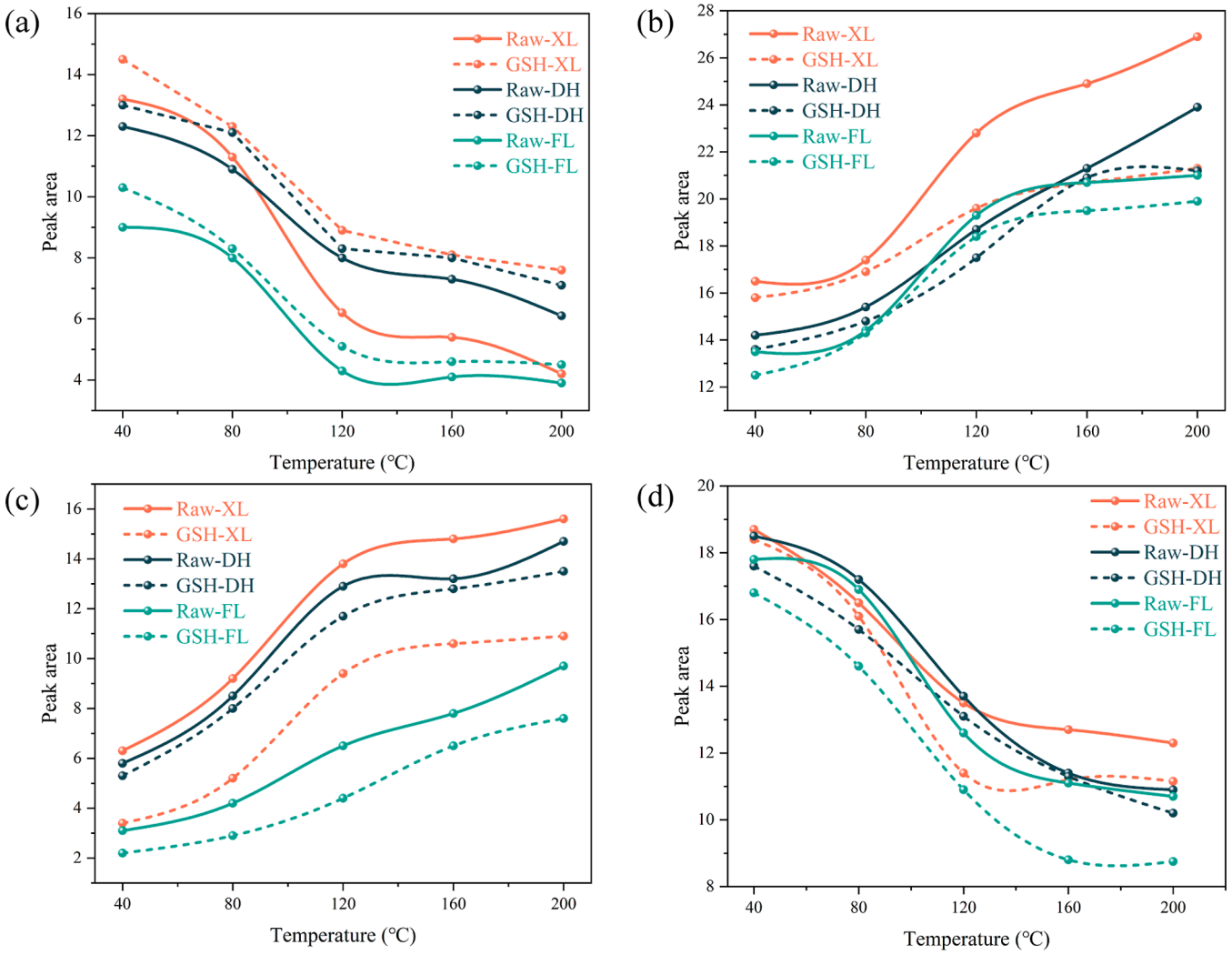

Figure 12. Variation law of (a) alkyl groups, (b) alkoxy groups, (c) carbonyl groups, and (d) hydroxyl groups in all samples.

explained by the reduction of the generation rates of alkoxy groups.

Figure 12c displays the variation pattern of carbonyl group contents with temperature increase for all samples. Primary carbonyl groups are mainly present in the primary aldehyde and carboxyl groups in coal molecules and can also be generated by oxidation reactions, while the escape of CO and CO_2 is the main consumption pathway. The carbonyl group production rate is much higher than the consumption rate in the range of 30−120 °C, resulting in the rapid increase of its content. After 120 °C, the chain reactions gradually form, and the increase of the carbonyl group consumption rate slows down the elevating trend. Comparing all samples, the carbonyl group contents of the inhibited samples are smaller than those of the raw samples, reflecting the inhibiting effects of GSH.

Figure 12d exhibits the variation law of hydroxyl group contents of all samples with the increase of temperature. As can be seen, the hydroxyl group contents in all samples gradually decrease with increasing temperature, mainly because the hydroxyl groups can react with the H atoms in the coal to form H_2O or continue to participate in other oxidation reactions. Moreover, the hydroxyl group contents of the inhibited samples are generally smaller than those of the raw samples, which is due to the accelerating effects on the hydroxyl group consumption of GSH. These observations appear to reflect the inhibiting effects of GSH.

3.5. Quantum Chemical Calculations Analysis.

3.5.1. Molecular Structure Optimization and Reactivity Analysis. Reactive sites are the most susceptible reaction sites during COLT.[56] In order to predict the reaction mechanism of GSH, the DFT method was applied to optimize the geometric structure of each reactive group, and the ESP distribution was used to predict the reactive sites. The results of the analysis in Multiwfn 3.7 software[57] are shown in Figure 13.

From previously published studies,[40] the ESP of the red region of the molecular structure is positive, and the darker the color is, the more likely it is that the nucleophilic reactions occur; while the ESP in the blue region is negative, and the darker the color is, the more likely it is that the electrophilic reactions occur.[55] Statistically, the reactive site and its ESP value of each molecule are shown in Table 3, and it can be seen that the ESP near the H37 atom of the GSH molecule is extremely large, which can readily provide electrons to react with the reactive groups and is a nucleophilic reagent. The ESP minima of $Ar-CH_2-OO^{\bullet}$, $Ar-CH_2-O^{\bullet}$, and $^{\bullet}OH$ are all located near the outermost O atoms, which are easily accessible to electrons and are electrophilic reagents. Similarly,

https://doi.org/10.1021/acsomega.2c03861
ACS Omega 2022, 7, 31448−31465

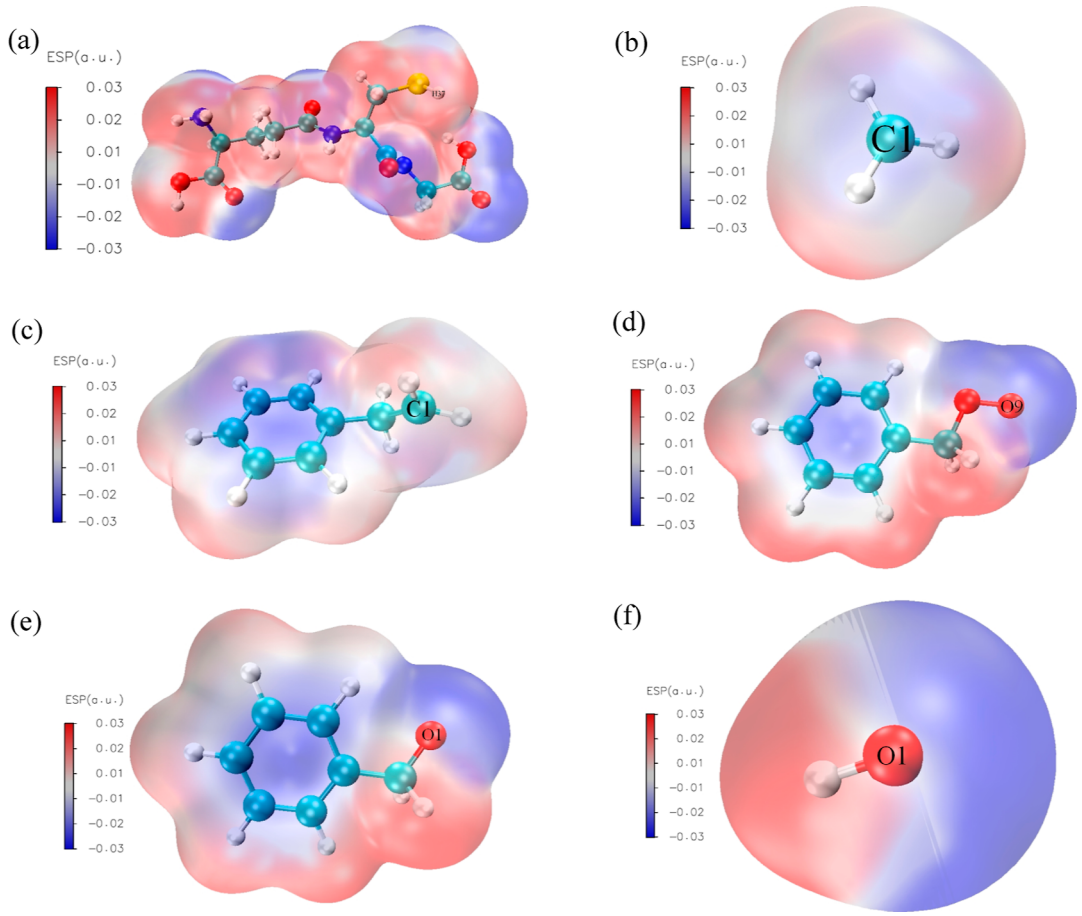

Figure 13. ESP isosurface maps of (a) GSH, (b) $^{\bullet}CH_3$, (c) Ar−CH_2−$^{\bullet}CH_2$, (d) Ar−CH_2−OO$^{\bullet}$, (e) Ar−CH_2−O$^{\bullet}$, and (f) $^{\bullet}$OH.

Table 3. Reactive Site and Its ESP Value of Each Molecule

categories	GSH	$^{\bullet}CH_3$	Ar−CH_2−$^{\bullet}CH_2$	Ar−CH_2−OO$^{\bullet}$	Ar−CH_2−O$^{\bullet}$	$^{\bullet}$OH
atom	H37	C1	O7	O9	O1	O1
ESP (kcal/mol)	54.90	−9.30	−7.68	−29.221	−21.19	−25.43

the ESP minima of $^{\bullet}CH_3$ are located near the C1 atom and can be considered as an electrophilic reagent. It is worth noting that although the ESP minimum of Ar−CH_2−$^{\bullet}CH_2$ is located near the benzene ring, the chemical bonds of the benzene ring are relatively stable and not easy to react, and the closed conjugated large π bonds will overlap each other laterally, making the chemical properties more stable, so the reactivity is lower than that of the side chain atoms. Therefore, its reactive site is located near the subminimal value point of the ESP, that is, the C1 atom, which is also an electrophilic reagent. From the results, it is clear that the ESP of the reactive groups are ordered as Ar−CH_2−OO$^{\bullet}$ > $^{\bullet}$OH > Ar−CH_2−O$^{\bullet}$ > $^{\bullet}CH_3$ > Ar−CH_2−$^{\bullet}CH_2$.

3.5.2. Molecular Frontier Orbital Analysis. The frontier orbital theory proposes that chemical reactions take place on account of the mutual attraction of the highest or the single occupied molecular orbital (HOMO/SOMO) and the lowest unoccupied molecular orbital (LUMO) or the SOMO between two reactants. Since electrons in the front orbitals are generally more active than others, they tend to trigger electrons transfer and cause bonding or bond breaking, which leads to the reaction. Consequently, the bonding properties of chemical reactions depend on the electron activity of the frontier orbital.[58] The GSH molecule is a nucleophilic reagent, its HOMO orbital easily loses electrons, and the reactive bond is covered by the largest electron cloud on the HOMO orbital; however, other reactive groups are electrophilic reagents, their SOMOs find it straightforward to obtain electrons, and the reactive bonds are covered by the largest electron cloud on the SOMO orbital. The results are shown in Figure 14.

From the figure, it can be seen that the largest electron cloud on the HOMO of the GSH molecule is located on the S−H bond, and the electron cloud is very abundant for its bond activity. The largest electron clouds on the SOMO of CH_3, Ar−CH_2−$^{\bullet}CH_2$, Ar−CH_2−OO$^{\bullet}$, Ar−CH_2−O$^{\bullet}$, and $^{\bullet}$OH are located on the C1, C1, O1, O9, and O1 atoms, respectively, as the reactive bonds. The enormous electron cloud of Ar−O$^{\bullet}$ is located on the benzene ring, but due to the stable properties of the benzene ring, the reactive bond is the largest electron cloud of the side chain atom, which is located on the O7 atom. The results of this analysis are identical to the ESP results, which mutually verified the accuracy.

3.5.3. IRC and Thermodynamic Parameter Calculations. 3.5.3.1. Reaction of $^{\bullet}CH_3$ Capturing the H Atom in GSH. Reaction 1 is the capture of the H atom in GSH by $^{\bullet}CH_3$. The TS (Berny) method is used to search the transition state

https://doi.org/10.1021/acsomega.2c03861
ACS Omega 2022, 7, 31448−31465

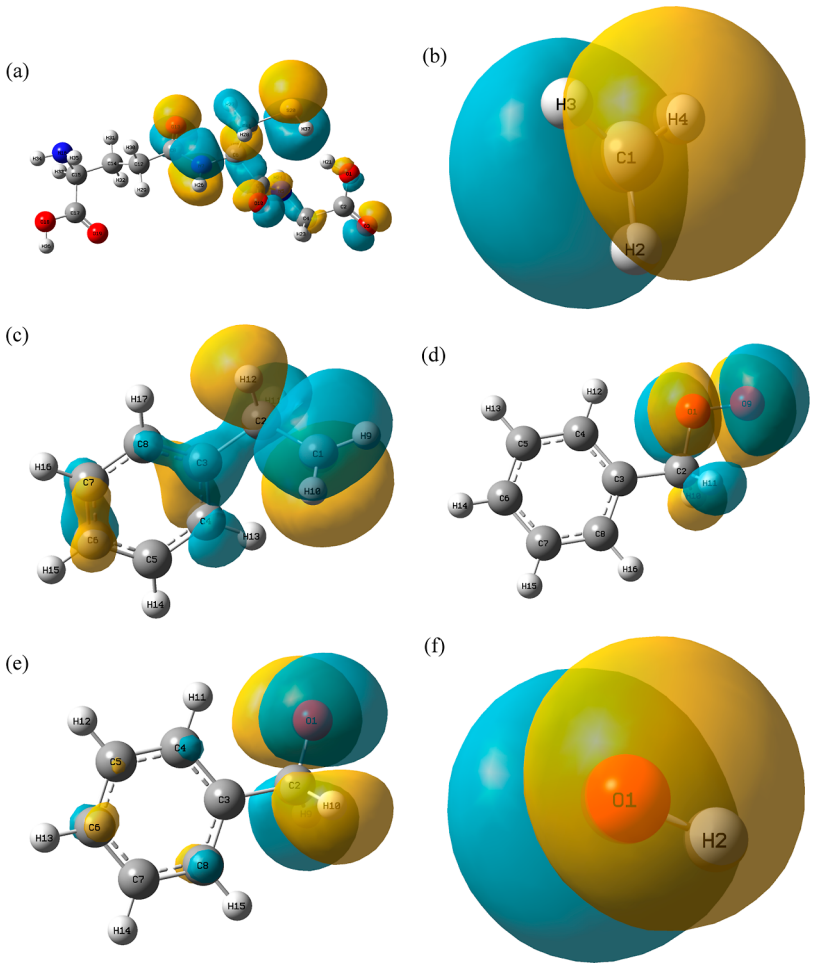

Figure 14. Electron cloud distribution in frontier molecular orbitals of (a) GSH, (b) $^{\bullet}CH_3$, (c) Ar−CH_2−$^{\bullet}CH_2$, (d) Ar−CH_2−$OO^{\bullet}$, (e) Ar−CH_2−$O^{\bullet}$, and (f) $^{\bullet}OH$.

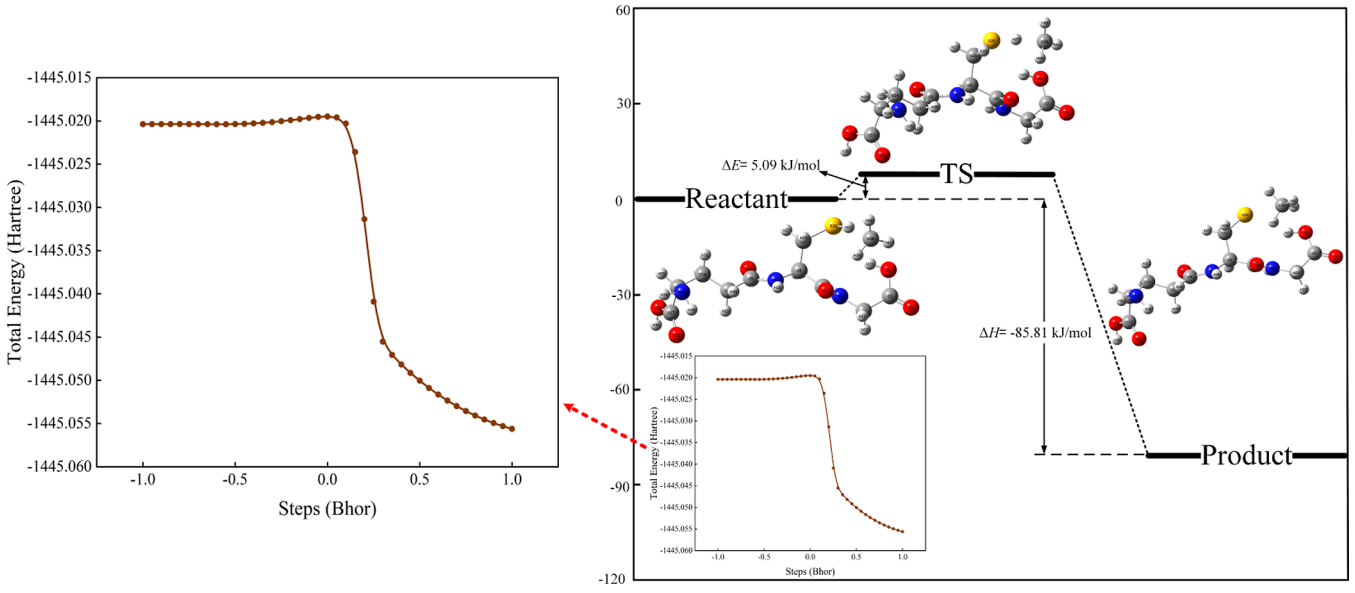

Figure 15. Molecular structures and thermodynamic parameters of Reaction 1.

structure and optimize it. As a result of the presence of one unpaired electron in the reaction system, the spin multiplicity is set to 2, and the calculated system is an open shell system. Calculation of the transition state shows the existence of a unique virtual frequency of −285.74, and the vibration direction corresponds the reactants and products, which verifies the accuracy of the transition state. Pathways calculations are performed using the IRC method, and the

https://doi.org/10.1021/acsomega.2c03861
ACS Omega 2022, 7, 31448−31465

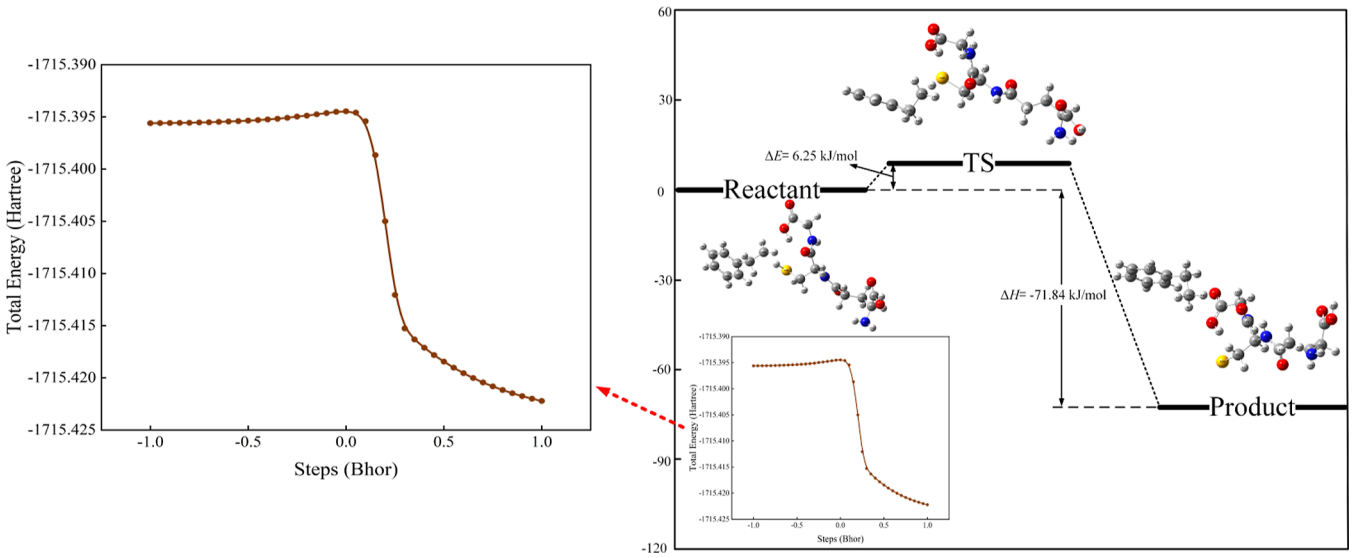

Figure 16. Total energy change and molecular structure of each stagnation point in Reaction 1.

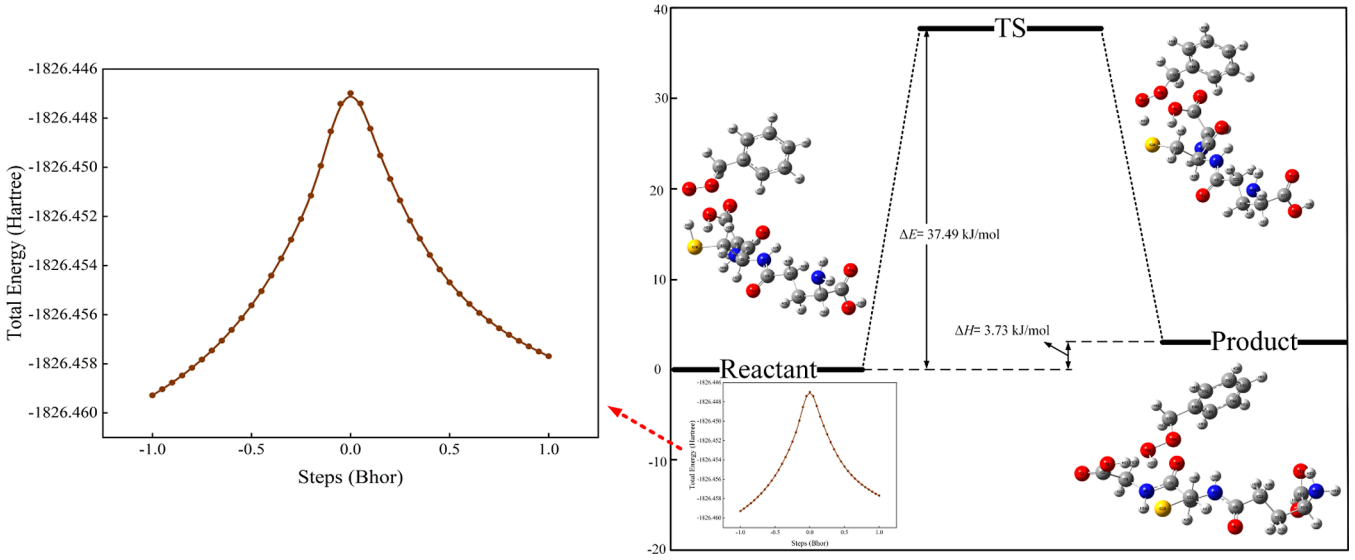

Figure 17. Total energy change and molecular structure of each stagnation point in Reaction 1.

forward of the IRC curve connects the products, while the reverse of the curve connects the reactants, both of which have no virtual frequencies, verifying the correctness of the reaction pathway. Figure 15 shows the molecular structures and thermodynamic parameters of Reaction 1.

The figure shows that the S−H bond breaking is the beginning of the reaction, so the S−H bond is the reactive bond, which is consistent with the conclusion obtained from the previous frontier orbital analysis and again verifies the correctness of the reaction pathway. In the reactants, the S20−H37 bond length is 1.36 Å, and it breaks when the absorbed energy reaches the reaction energy barrier, with the H37 atom gradually moving away from the S20 atom and toward the C38 atom. The transition state forms when the equilibrium distance between S20 and H17 atoms reaches 1.48 Å. Eventually the H37 atom forms a C−H bond with the C38 atom, and the C38 atom changes from sp^2 hybridization to sp^3 hybridization. In the meantime, the overall configuration changes from the original planar structure to a positive tetrahedral structure, forming CH4, which will escape from the coal under the influence of temperature. Soon afterward, the bond angle of C11−S20−H37 becomes 96.33° in the reactants and reverses to 86.78° in the products. The reaction requires overcoming a reaction energy barrier of 5.09 kJ/mol, indicating that GSH has a wide range of temperature applicability and can play a crucial role in inhibiting the COLT. The reaction gives off a total heat of 85.81 kJ/mol, which has a low thermal effect and does not contribute significantly to the absorption of heat by the coal itself.

3.5.3.2. Reaction of Ar−CH_2−•CH_2 Capturing the H Atom in GSH. The same method is applied to search the transition state configuration, and the spin multiplicity is set to 2. The calculation shows that there is a unique virtual frequency of −323.49 for this reaction, and the forward end of the IRC curve connects the products and the reverse end connects the reactants, both of which have no virtual frequency, verifying the correctness of the reaction pathway. The total energy change and molecular structure of each stagnation point in Reaction 1 are exhibited in Figure 16.

https://doi.org/10.1021/acsomega.2c03861
ACS Omega 2022, 7, 31448−31465

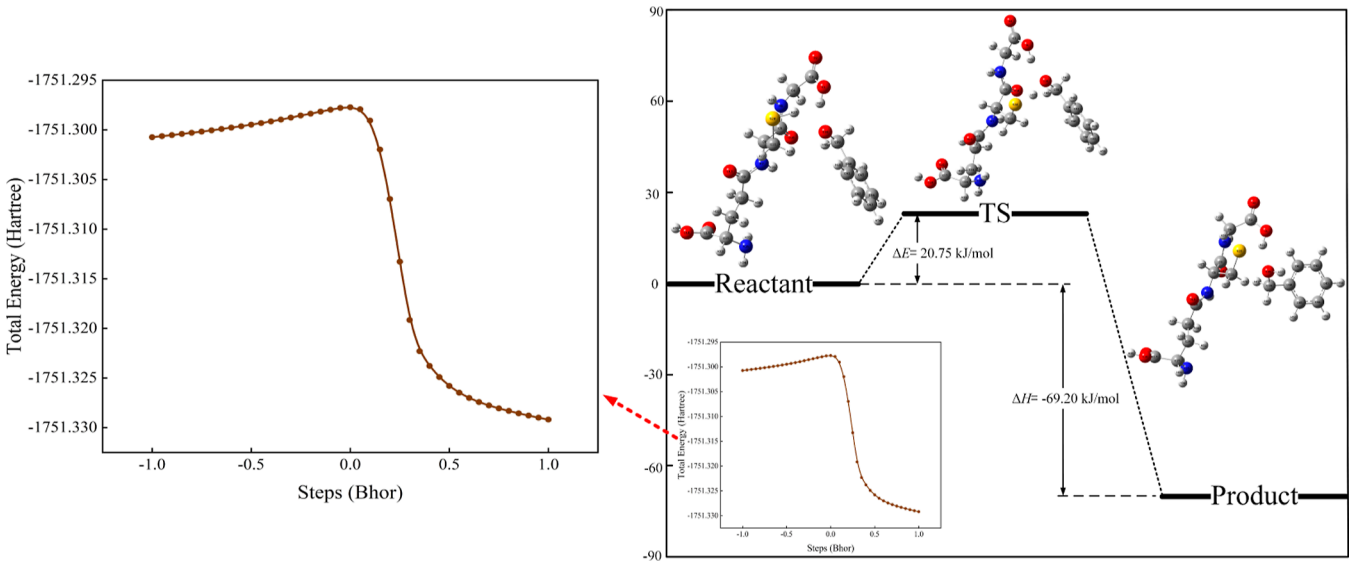

Figure 18. Total energy change and molecular structure of each stagnation point in Reaction 1.

Observations of the structure of each stationary point and calculation of their thermodynamic parameters show that the reaction mechanism is correct and feasible. During the reaction, the reaction mechanism of the GSH molecule is the same as that of Reaction 1, which also starts with the breaking of the S20−H37 bond (reactant, $R_{S20-H37}$ = 1.36 Å), and its equilibrium distance gradually increases to 1.44 Å (transition state). As the reaction proceeds, the H37 atom continues to move toward the C38 atom and forms a covalent bond with a bond length of 1.09 Å (product). The C38 atom changes from sp^2 hybridization to sp^3 hybridization after getting the H37 atom, so the C38−H37 bond is a σ bond formed by s−sp^3 hybridization. At the same time, the bond angle of H46−C38−H47 in Ar−CH_2−$^{\bullet}CH_2$ reverses from 117.44 to 108.18°, and the microscopic parameters of the products are all consistent with the known −CH_3 parameters, indicating that the H37 atom has completely detached from GSH to form −CH_3 and reached the stable state. The reaction has an activation energy of 37.49 kJ/mol and releases 3.73 kJ/mol of heat, indicating that the reaction can proceed at room temperature or higher with a low thermal effect.

3.5.3.3. Reaction of Ar−CH_2−$OO^{\bullet}$ Capturing the H Atom in GSH. Similarly, the reaction spin multiplicity is set to 2. After calculation, the unique virtual frequency of −1462.44 and the IRC curve verify the accuracy of the reaction pathway. The total energy change and molecular structure of each stagnation point in Reaction 1 are shown in Figure 17.

The reaction is made up of the breaking of the S−H bond and the formation of the O−H bond. In the ground state of the reactants, the S20−H37 bond length is 1.35 Å, and with the absorption of heat, the bond breaks and the H37 atom separates from the S20 atom. Subsequently, the H37 atom gradually moves toward the O46 atom under the attraction of the charge carrying of $-OO^{\bullet}$, and in the transition state, the equilibrium distance between S20 and H37 reaches 1.59 Å, which is larger than the equilibrium distance between O46 and H37 of 1.20 Å. As the H37 atom continues to move, the O−H covalent bond gradually forms with a bond length of 0.97 Å. In the subsequent reaction, the O55−O56 bond increases from 1.36 to 1.47 Å, indicating that the bond could be broken by heat to form oxygen radicals and hydroxyl radicals. Although the products were both reactive radicals, both could continue to be reduced by GSH molecules to form stable compounds. The whole reaction requires overcoming an energy barrier of 37.49 kJ/mol, which again indicates that the reaction could proceed spontaneously at room temperature, reflecting the effectiveness of GSH as an antioxidant. The enthalpy change is 3.73 kJ/mol, which is a heat absorbing reaction that could reduce the self-heating of the coal.

3.5.3.4. Reaction of Ar−CH_2−$O^{\bullet}$ Capturing the H Atom in GSH. After calculation, the spin multiplicity of the reaction can be considered to be 2, and the unique virtual frequency is −1462.44. Simultaneously, the IRC curve verifies the accuracy of the reaction pathway. The total energy change and molecular structure of each stagnation point in Reaction 1 are displayed in Figure 18.

It can be seen that before the reaction occurs, Ar−CH_2−$O^{\bullet}$ is adsorbed near the GSH molecule, and the oxygen radical is located exactly at the ESP maximum of GSH. The bond length of the S20−H37 bond in this state is 1.35 Å, and the O38−C39 bond is in the same plane as the benzene ring to which it is attached. As the reaction system reaches the transition state, the equilibrium distance between S20 and H37 reaches 1.44 Å. The covalent bond formed between S20 and H37 has broken, indicating that the H37 atom is gradually moving toward the O38 atom. Upon the completion of the reaction, H37 forms a covalent bond with the O38 atom with a bond length of 0.97 Å, while the linear angle of the O38−C39 bond with the attached benzene ring reverses from 0 to 133.01°. The activation energy of the reaction is 20.75 kJ/mol and the enthalpy change is 69.20 kJ/mol, which indicates that the reaction requires very low heat and can occur at room temperature and pressure. Furthermore, the small heat release has a small effect on the self-heating of coal, reflecting the wide range of application of GSH.

3.5.3.5. Reaction of $^{\bullet}OH$ Capturing the H Atom in GSH. After calculation, the spin multiplicity of the reaction can be considered to be 2, and the unique virtual frequency is −1776.50. Simultaneously, the IRC curve verifies the accuracy of the reaction pathway. The total energy change and molecular structure of each stagnation point in Reaction 1 are displayed in Figure 19.

https://doi.org/10.1021/acsomega.2c03861
ACS Omega 2022, 7, 31448−31465

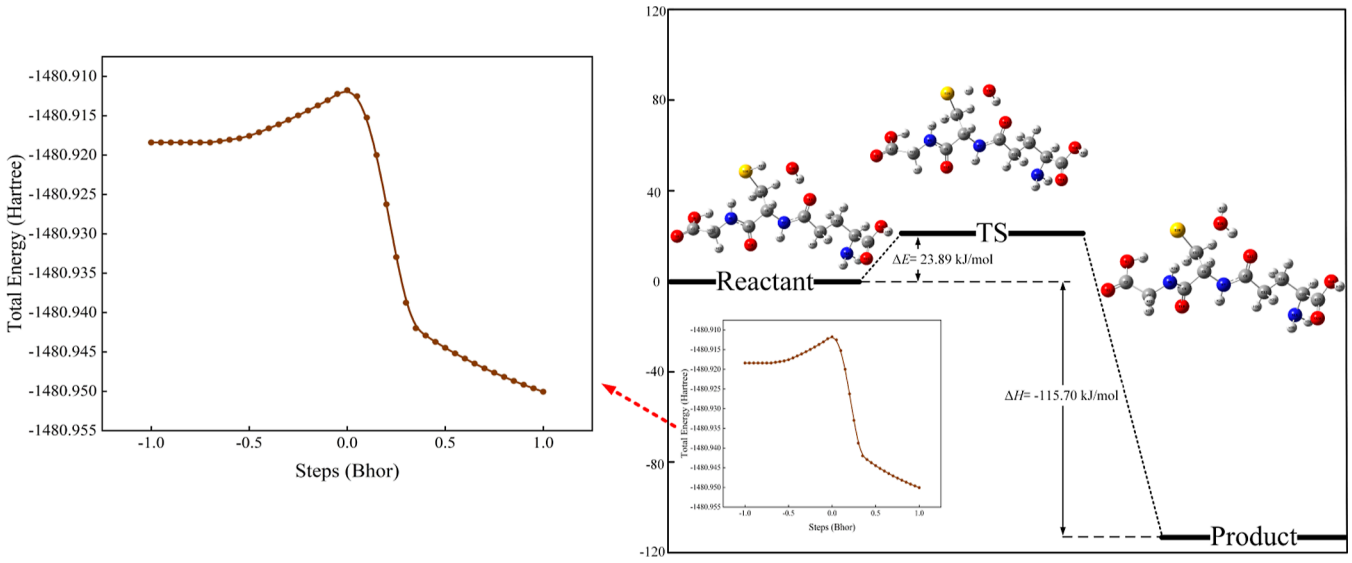

Figure 19. Total energy change and molecular structure of each stagnation point in Reaction 1.

The structural parameters of each molecule change during the reaction are as follows: the S20−H37 bond length gradually increases, resulting in the covalent bond break, and the H37 atom breaks away from the adsorption of the S20 atom. Compared with that of the reactant and transition state, the O38−H37 bond of the product is further shortened, while the O38−H39 bond remains essentially unchanged, with the lengths stabilizing at 0.973 Å. The bond angle of H39−O38−H37 gradually decreases from 105.82 to 104.48°, which is essentially consistent with the empirical value of the H_2O molecular structure, indicating that the H_2O molecule has completely formed an independent and stable structure. The 2s, $2p_x$, $2p_y$, and $2p_z$ atomic orbitals of the O42 atom are all sp^3 hybridized, two of which are occupied by two pairs of lone pairs of electrons, and the other two form σ bonds with H37 and H39 atoms. At the same time, due to the dense electron cloud of the hybrid orbital occupied by the lone pair of electrons, the hybrid orbital occupied by the bonding electron pair plays a role in shoving and compressing so that the bond angle of two O−H bonds is compressed to 104.48°, forming a V-shaped structure. The activation energy required for the reaction is very small, only 23.89 kJ/mol, and the enthalpy change is −115.70 kJ/mol, which is an exothermic reaction. The results clarify that the reaction can proceed spontaneously at normal temperature and pressure, and it has some effects of enhancing the self-heating of the coal.

3.5.3.6. Polymerization Reaction between GS•. The reaction is a polymerization reaction. Since the reaction does not involve bond breaking and only the bonding process exists, there is no transition state and activation energy, and it can proceed spontaneously at room temperature and pressure. After optimization, both the reactant and product molecules have no virtual frequency, which verifies the accuracy of the optimization process. The total energy change and the molecular structure of each stationary point in Reaction 1 are shown in Figure 20.

After the statistics of the molecular structure parameters, it can be seen that the two molecules in the reactant are symmetrically distributed, where the equilibrium distance between S20 and S56 is 2.65 Å and the bond angle of C11−S20−S56 is 95.73°. As the reaction proceeds, the two

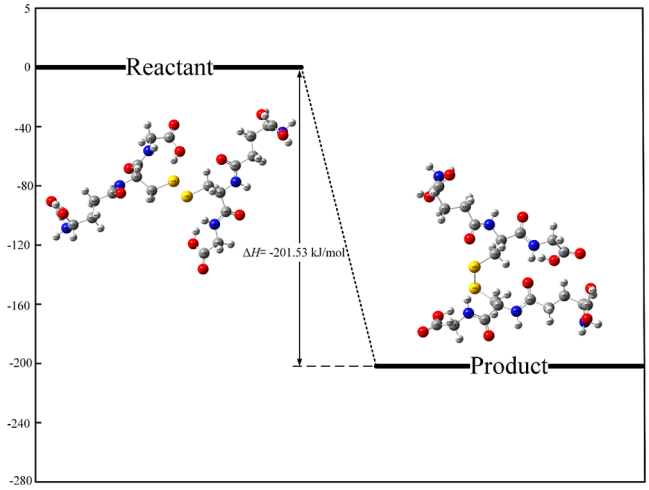

Figure 20. Total energy change and molecular structure of each stagnation point in Reaction 1.

molecules move in opposite directions and twist, a disulfide bond forms between the S20 and S56 atoms, and the product of this reaction, GSSH, reaches a steady state. The S20−S56 bond length in GSSH is 2.10 Å, while the bond angle of C11−S20−S56 increases to 100.61°. The enthalpy change of the reaction is −201.53 kJ/mol, indicating that the reaction is exothermic and exerts a large amount of heat.

4. INHIBITING MECHANISM OF GSH ON THE CHAIN REACTION OF COLT

Through the combined analyses of data from the above study, the inhibiting pathway of GSH can be summarized as shown in Figure 21.

The blue line in the figure illustrates the evolution pathway of the reactive groups during the COLT. It is found that in the chain initiation stage, the original $R-CH_3$ is mechanically broken or geothermally heated to produce a large number of $R-{}^{\bullet}CH_2$ radicals, which can undergo chemisorption reactions with O_2 to form $R-CH_2-OO^{\bullet}$. $R-CH_2-OO-$ is highly oxidizing and can capture the H atom in the original reactive groups to generate $R-CH_2-OOH$ in the chain propagation

https://doi.org/10.1021/acsomega.2c03861
ACS Omega 2022, 7, 31448−31465

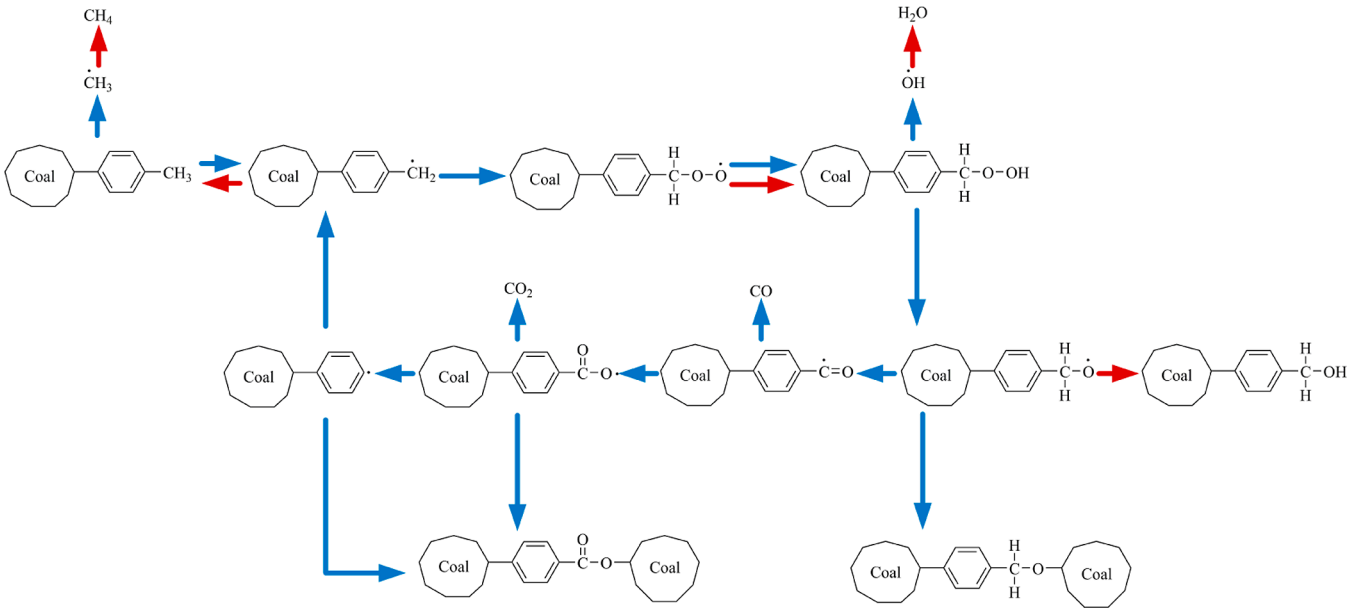

Figure 21. Inhibition mechanism and process of GSH on the chain reaction of COLT.

stage. R−CH_2−OOH is not stable and could form R−CH_2−O$^\bullet$ and $^\bullet$OH under the action of temperature. Among them, $^\bullet$OH can also seize the H atom in the reactive group to promote the chain reaction, while R−CH_2−O$^\bullet$ can be further oxidized to R−$^\bullet$C═O and R−C═O(−O$^\bullet$) and undergo decarbonylation and decarboxylation reactions to produce CO and CO_2. The other products of the decarbonylation and decarboxylation reactions are R$^\bullet$, who on one hand can continue to participate in the chain reaction as reactive groups and on the other hand can polymerize with R−CH_2−O$^\bullet$ and R−C═O(−O$^\bullet$) in the chain termination stage to form stable ether bonds. It is to be noted that $^\bullet CH_3$ is directly removed from R−CH_3 under the action of high temperature and becomes a reactive group to participate in the chain reaction.

The red line in the figure illustrates the inhibiting pathway of GSH during the COLT. In the chain initiation stage, GSH can first act on R−$^\bullet CH_2$ radicals and hinder the chemisorption reaction of R−$^\bullet CH_2$ with O_2. Subsequently, GSH can react with R−CH_2−OO$^\bullet$ and gradually consume $^\bullet$OH, thus delaying the generation of the chain reaction. In the chain propagation stage, GSH can further act on R−CH_2−O$^\bullet$ to produce the more stable R−CH_2−OH. At higher temperatures, GSH can similarly reduce $^\bullet CH_3$ to CH_4 to escape directly, weakening the strength of the chain reaction. In addition to the above reaction mechanism, after GSH reduces the reactive groups to inactive material to generate GS$^\bullet$, a polymerization reaction between them occurs to generate GSSH with low activity to terminate the chain reaction.

On the whole, the inhibiting effect of GSH lies in inhibiting the chain reaction process of reactive radicals.

5. CONCLUSIONS

In this paper, the inhibiting characteristics of GSH on COLT were investigated through experimental methods, and the inhibiting mechanism of GSH was also revealed using quantum chemical calculations. The following conclusions were mainly obtained:

(1) Compared with the raw coal samples, the GSH-treated samples show lower CO and CO_2 production and less O_2 consumption during the heating process. In addition, GSH can effectively delay the CPTs of coal samples. By calculating the inhibiting rates, we can find that the main action temperature of GSH is 60−150 °C, and the lower the degree of coal deterioration, the better the inhibiting effects of GSH.

(2) GSH can effectively enhance the characteristic temperature point of raw coal and reduce the exothermic power in the COLT, and it has good applicability for lignite, long-flame coal, and fatty coal.

(3) GSH, as an inhibitor, can change the content of functional groups in coal. It mainly increases the content of alkyl groups and decreases the contents of alkoxy, carbonyl, and carboxyl groups. In addition, it is known from EPR experiments that GSH can reduce the content of reactive radicals in coal.

(4) The inhibition of GSH is brought about by inerting the reactive radicals by the H atom of the S−H bond in GSH. At the same time, GSSH with stable properties can be produced by the polymerization between GS$^\bullet$ after the loss of the H atom in GSH. The activation energy of each reaction is very small and can occur at normal temperature and pressure.

AUTHOR INFORMATION

Corresponding Author

Hongqing Zhu − *School of Emergency Management and Safety Engineering, China University of Mining and Technology (Beijing), Beijing 100083, China;* Email: zhqcumtb1@163.com

Author

Yujia Huo − *School of Emergency Management and Safety Engineering, China University of Mining and Technology (Beijing), Beijing 100083, China;* orcid.org/0000-0001-9432-6164

Complete contact information is available at: https://pubs.acs.org/10.1021/acsomega.2c03861

https://doi.org/10.1021/acsomega.2c03861
ACS Omega 2022, 7, 31448−31465

Author Contributions

H.Z.: review and editing. Y.H.: writing the original draft, experiments and simulation methods, and data arrangement.

Notes

The authors declare no competing financial interest.

■ ACKNOWLEDGMENTS

This study was funded by the National Natural Science Foundation of China (grant no. 51704299, grant no. 51804311, and grant no. 52074304).

■ REFERENCES

(1) Li, Y.; Hu, X.; Cheng, W.; Shao, Z.; Xue, D.; Zhao, Y.; Lu, W. A novel high-toughness, organic/inorganic double-network fire-retardant gel for coal-seam with high ground temperature. *Fuel* **2020**, *263*, 116779.

(2) Nimaje, D. S.; Tripathy, D. P. Characterization of some Indian coals to assess their liability to spontaneous combustion. *Fuel* **2016**, *163*, 139−147.

(3) Onifade, M.; Genc, B. Spontaneous combustion of coals and coal-shales. *Int. J. Min. Sci. Technol.* **2018**, *28*, 933−940.

(4) Shi, X.; Zhang, Y.; Chen, X.; Zhang, Y. Effects of thermal boundary conditions on spontaneous combustion of coal under temperature-programmed conditions. *Fuel* **2021**, *295*, 120591.

(5) Huo, Y.; Zhu, H.; He, X.; Fang, S.; Wang, W. Quantum Chemistry Calculation Study on Chain Reaction Mechanisms and Thermodynamic Characteristics of Coal Spontaneous Combustion at Low Temperatures. *ACS Omega* **2021**, *6*, 30841−30855.

(6) Song, Z.; Wu, D.; Jiang, J.; Pan, X. Thermo-solutal buoyancy driven air flow through thermally decomposed thin porous media in a U-shaped channel: Towards understanding persistent underground coal fires. *Appl. Therm. Eng.* **2019**, *159*, 113948.

(7) Song, Z.; Huang, X.; Jiang, J.; Pan, X. A laboratory approach to CO2 and CO emission factors from underground coal fires. *Int. J. Coal Geol.* **2020**, *219*, 103382.

(8) Guo, S.; Yan, Z.; Yuan, S.; Weile, G. Inhibitory effect and mechanism of l-ascorbic acid combined with tea polyphenols on coal spontaneous combustion. *Energy* **2021**, *229*, 120651.

(9) Wang, H.; Tan, B.; Shao, Z.; Guo, Y.; Zhang, Z.; Xu, C. Influence of different content of FeS_2 on spontaneous combustion characteristics of coal. *Fuel* **2021**, *288*, 119582.

(10) Miao, G.; Li, Z.; Meng, Q.; Li, J.; Yang, Y. Experimental research on the emission of higher molecular weight gases during coal oxidation. *Fuel* **2021**, *300*, 120906.

(11) Song, J.-J.; Deng, J.; Zhao, J.-Y.; Zhang, Y.-N.; Shu, C.-M. Comparative analysis of exothermic behaviour of fresh and weathered coal during low-temperature oxidation. *Fuel* **2021**, *289*, 119942.

(12) Zhang, L.; Li, Z.; He, W.; Li, J.; Qi, X.; Zhu, J.; Zhao, L.; Zhang, X. Study on the change of organic sulfur forms in coal during low-temperature oxidation process. *Fuel* **2018**, *222*, 350−361.

(13) Qu, Z.; Sun, F.; Gao, J.; Pei, T.; Qie, Z.; Wang, L.; Pi, X.; Zhao, G.; Wu, S. A new insight into the role of coal adsorbed water in low-temperature oxidation: Enhanced $^{\bullet}OH$ radical generation. *Combust. Flame* **2019**, *208*, 27−36.

(14) Fei, Y.; Aziz, A. A.; Nasir, S.; Jackson, W. R.; Marshall, M.; Hulston, J.; Chaffee, A. L. The spontaneous combustion behavior of some low rank coals and a range of dried products. *Fuel* **2009**, *88*, 1650−1655.

(15) Tan, B.; Cheng, G.; Fu, S.; Wang, H.; Li, Z.; Zhang, X. Molecular simulation for physisorption characteristics of O_2 in low-rank coals. *Energy* **2022**, *242*, 122538.

(16) Cheng, G.; Tan, B.; Zhang, Z.; Fu, S.; Haiyan, W.; Wang, F. Characteristics of coal-oxygen chemisorption at the low-temperature oxidation stage: DFT and experimental study. *Fuel* **2022**, *315*, 123120.

(17) Chen, L.; Qi, X.; Tang, J.; Xin, H.; Liang, Z. Reaction pathways and cyclic chain model of free radicals during coal spontaneous combustion. *Fuel* **2021**, *293*, 120436.

(18) Zhu, H.; Huo, Y.; He, X.; Wang, W.; Fang, S.; Zhang, Y. Molecular model construction of Danhou lignite and study on adsorption of CH4 by oxygen functional groups. *Environ. Sci. Pollut. Res. Int.* **2021**, *28*, 25368−25381.

(19) Li, J.; Li, Z.; Yang, Y.; Zhang, X.; Yan, D.; Liu, L. Inhibitive Effects of Antioxidants on Coal Spontaneous Combustion. *Energy Fuels* **2017**, *31*, 14180−14190.

(20) Yang, Y.; Li, Z.; Si, L.; Hou, S.; Zhou, Y.; Qi, Q. Consolidation grouting technology for fire prevention in mined-out areas of working face with large inclined angle and its application. *Fire Mater.* **2017**, *41*, 700−715.

(21) Zhu, H.; Wang, W.; Huo, Y.; He, X.; Zhao, H.; Wang, H. Molecular Simulation Study on Adsorption and Diffusion Behaviors of CO2/N2 in Lignite. *ACS Omega* **2020**, *5*, 29416−29426.

(22) Zhu, H.; He, X.; Xie, Y.; Guo, S.; Huo, Y.; Wang, W. A Study on the Effect of Coal Metamorphism on the Adsorption Characteristics of a Binary Component System: CO2 and N2. *ACS Omega* **2021**, *6*, 523−532.

(23) Lu, X.-x.; Xing, Y.; Shen, C.; Li, Y.-b.; Wang, M.-y.; Liu, J.-p. The characteristic research on the flame retardant of calcification foam on the high temperature coal. *Adv. Powder Technol.* **2022**, *33*, 103359.

(24) Lu, X.; Zhu, H.; Wang, D.; Hu, C.; Zhao, H.; Huo, Y. Flow characteristic investigation of inhibition foam used for fire extinguishment in the underground goaf. *Process Saf. Environ. Prot.* **2018**, *116*, 159−168.

(25) Qi, X.; Wei, C.; Li, Q.; Zhang, L. Controlled-release inhibitor for preventing the spontaneous combustion of coal. *Nat. Hazards* **2016**, *82*, 891−901.

(26) Wang, D.; Dou, G.; Zhong, X.; Xin, H.; Qin, B. An experimental approach to selecting chemical inhibitors to retard the spontaneous combustion of coal. *Fuel* **2014**, *117*, 218−223.

(27) Lv, H.; Li, B.; Deng, J.; Ye, L.; Gao, W.; Shu, C.-M.; Bi, M. A novel methodology for evaluating the inhibitory effect of chloride salts on the ignition risk of coal spontaneous combustion. *Energy* **2021**, *231*, 121093.

(28) Guo, B.; Liang, Y.; Qi, G.; Lu, W.; Tian, F.; Sun, Y.; Song, S. Research on the qualitative and quantitative analysis of the physical and chemical inhibition effect of coal seam inhibitors. *Fuel* **2022**, *310*, 122482.

(29) Du, W.; Zhang, J.; Xie, Q.; Zhang, Y.; Niu, K.; Wang, H. Experimental study on optimizing the inhibition effect of pre-injection inhibitor on coal spontaneous combustion. *Energy Sources, Part A* **2020**, *0*, 1−18.

(30) Pan, R.; Ma, J.; Fu, D.; Li, C.; Jia, H.; Zheng, L. Experimental study on the new environmental protection chemical composite inhibitor for the inhibition of coal spontaneous combustion. *J. Therm. Anal. Calorim.* **2019**, *139*, 37−45.

(31) Ma, L.; Wang, D.; Wang, Y.; Dou, G.; Xin, H. Synchronous thermal analyses and kinetic studies on a caged-wrapping and sustained-release type of composite inhibitor retarding the spontaneous combustion of low-rank coal. *Fuel Process. Technol.* **2017**, *157*, 65−75.

(32) Shi, Q.; Qin, B.; Xu, Y.; Hao, M.; Shao, X.; Zhuo, H. Experimental investigation of the drainage characteristic and stability mechanism of gel-stabilized foam used to extinguish coal fire. *Fuel* **2022**, *313*, 122685.

(33) Xi, Z.; Jin, B.; Jin, L.; Li, M.; Li, S. Characteristic analysis of complex antioxidant enzyme inhibitors to inhibit spontaneous combustion of coal. *Fuel* **2020**, *267*, 117301.

(34) Xi, Z.; Jin, B.; Shan, Z. Reaction mechanisms involving peroxy radical in the low-temperature oxidation of coal. *Fuel* **2021**, *300*, 120943.

(35) Li, J.; Li, Z.; Yang, Y.; Kong, B.; Wang, C. Laboratory study on the inhibitory effect of free radical scavenger on coal spontaneous combustion. *Fuel Process. Technol.* **2018**, *171*, 350−360.

https://doi.org/10.1021/acsomega.2c03861
ACS Omega 2022, 7, 31448−31465

(36) Lu, W.; Sun, X.; Gao, L.; Hu, X.; Song, H.; Kong, B. Study on the characteristics and mechanism of DL-malic acid in inhibiting spontaneous combustion of lignite and bituminous coal. *Fuel* **2022**, *308*, 122012.
(37) Liu, P.; Li, Z.; Zhang, X.; Li, J.; Miao, G.; Cao, S.; Li, S. Study on the inhibition effect of citric acid on coal spontaneous combustion. *Fuel* **2022**, *310*, 122268.
(38) Dou, G.; Wang, D.; Zhong, X.; Qin, B. Effectiveness of catechin and poly(ethylene glycol) at inhibiting the spontaneous combustion of coal. *Fuel Process. Technol.* **2014**, *120*, 123−127.
(39) Wang, D.; Xin, H.; Qi, X.; Dou, G.; Qi, G.; Ma, L. Reaction pathway of coal oxidation at low temperatures: a model of cyclic chain reactions and kinetic characteristics. *Combust. Flame* **2016**, *163*, 447−460.
(40) Huo, Y.; Zhu, H.; He, X.; Fang, S.; Wang, W. Quantum Chemical Calculation of the Effects of H_2O on Oxygen Functional Groups during Coal Spontaneous Combustion. *ACS Omega* **2021**, *6*, 25594−25607.
(41) Zhu, H.; Huo, Y.; Wang, W.; He, X.; Fang, S.; Zhang, Y. Quantum chemical calculation of reaction characteristics of hydroxyl at different positions during coal spontaneous combustion. *Process Saf. Environ. Prot.* **2021**, *148*, 624−635.
(42) Zhu, H.; Huo, Y.; Fang, S.; He, X.; Wang, W.; Zhang, Y. Quantum Chemical Calculation of Original Aldehyde Groups Reaction Mechanism in Coal Spontaneous Combustion. *Energy Fuels* **2020**, *34*, 14776−14785.
(43) Deponte, M. Glutathione catalysis and the reaction mechanisms of glutathione-dependent enzymes. *Biochim. Biophys. Acta* **2013**, *1830*, 3217−3266.
(44) Couto, N.; Wood, J.; Barber, J. The role of glutathione reductase and related enzymes on cellular redox homoeostasis network. *Free Radicals Biol. Med.* **2016**, *95*, 27−42.
(45) Guo, Q.; Li, T.; Yuan, C.; Liang, L.; Gänzle, M. G.; Zhao, M. Effects of protein fibrillation and antioxidants on probiotic survival during ambient storage. *Food Chem.* **2022**, *389*, 133117.
(46) Reiter, R.; Tan, D.; Rosales-Corral, S.; Galano, A.; Zhou, X.; Xu, B. Mitochondria: Central Organelles for Melatonin's Antioxidant and Anti-Aging Actions. *Molecules* **2018**, *23*, 509.
(47) Adamus, A.; Šancer, J.; Guřanová, P.; Zubiček, V. An investigation of the factors associated with interpretation of mine atmosphere for spontaneous combustion in coal mines. *Fuel Process. Technol.* **2011**, *92*, 663−670.
(48) Liu, J.; Jiang, X.; Han, X.; Shen, J.; Zhang, H. Chemical properties of superfine pulverized coals. Part 2. Demineralization effects on free radical characteristics. *Fuel* **2014**, *115*, 685−696.
(49) Jin, B. *Study on reaction mechanism of antioxidant inhibiting coal peroxyradical based on quantum chemical*; Tianjin University of Technology, 2021.
(50) Wang, D. *The coal oxidation dynamics theory and application*; Science press: Beijing, 2012.
(51) Shi, T.; Wang, X.; Deng, J.; Wen, Z. The mechanism at the initial stage of the room-temperature oxidation of coal. *Combust. Flame* **2005**, *140*, 332−345.
(52) Yu, S.; Bo, J.; Fengjuan, L. Competitive adsorption of CO2/N2/CH4 onto coal vitrinite macromolecular: Effects of electrostatic interactions and oxygen functionalities. *Fuel* **2019**, *235*, 23−38.
(53) Grimme, S. Density functional theory with London dispersion corrections. *Wiley Interdiscip. Rev.: Comput. Mol. Sci.* **2011**, *1*, 211−228.
(54) Lu, T.; Chen, F. Quantitative analysis of molecular surface based on improved Marching Tetrahedra algorithm. *J. Mol. Graphics Modell.* **2012**, *38*, 314−323.
(55) Deng, J.; Li, Y.; Zhang, Y.; Yang, C.; Zhang, J.; Shi, X. Effects of hydroxyl on oxidation characteristics of side chain active groups in coal. *J. China Coal Soc.* **2020**, *45*, 232−240.
(56) Hagelin, H.; Murray, J. S.; Politzer, P.; Brinck, T.; Berthelot, M. Family-independent relationships between computed molecular surface quantities and solute hydrogen bond acidity/basicity and solute-induced methanol O−H infrared frequency shifts. *Can. J. Chem.* **1995**, *73*, 483−488.
(57) Lu, T.; Chen, F. Multiwfn: a multifunctional wavefunction analyzer. *J. Comput. Chem.* **2012**, *33*, 580−592.
(58) Li, X.; Tang, Y.; Wang, C.; Zhang, H.; Cheng, X. A DFT Investigation on Hydrogen Adsorption Based on Alkali-metal Organic Complexes. *Chin. J. Struct. Chem.* **2010**, *29*, 1404−1410.

https://doi.org/10.1021/acsomega.2c03861
ACS Omega 2022, 7, 31448−31465